

**Dissertation**  
**submitted to the**  
**Combined Faculties for Natural Sciences and for**  
**Mathematics**  
**of the Ruperto-Carola University of Heidelberg, Germany**  
**for the degree of**  
**Doctor of Natural Sciences**

**Put forward by**

**Dipl. Phys.:           Sonja Lahrmann**

**Born in:               Altena, Germany**

**Oral examination:   April 18, 2012**



# **Investigation of a scintillating screen detector for ion beam therapy**

**Referees: Prof. Dr. U. Oelfke  
Prof. Dr. C. Karger**





# **Abstract**

## **Investigation of a scintillating screen detector for ion beam therapy**

Scanned heavy ion radiotherapy produces complex dose distributions, which have to be measured with high resolution in quality assurance. This work investigates a scintillating screen detector, originally developed for beam diagnosis, for fluence measurements at the Heidelberg Ion-Beam Therapy Center (HIT). Measurement control and evaluation software was developed, implemented and used to investigate background, camera settings, influence of the lens and the 45° tilt of the screen relative to the beam on the image signal. Correction methods for background, vignetting and perspective were developed and applied for detector response measurements. The signal of the detector is independent on beam intensity and shows a strictly linear dependence on fluence with an energy-dependent slope. As the fluence calibration showed large day-by-day variations, a recalibration is required for each measurement session. Comparisons of measured and calculated 2d fluence maps of treatment plans showed broader distributions in the measurement. This was attributed to an optical blurring effect, which has not been corrected for and has to be further investigated before the system can be used clinically. In conclusion, a method for vignetting and perspective correction was developed and the system was characterized for different beam parameters. Finally, requirements for an optimized system were derived.

# **Zusammenfassung**

## **Untersuchung eines Leuchtschirm-Detektors für die Schwerionentherapie**

Die Schwerionentherapie im Rasterscanverfahren erzeugt komplexe Dosisverteilungen, die im Rahmen der Qualitätssicherung mit hoher Auflösung gemessen werden müssen. In dieser Arbeit wurde ein Leuchtschirm-Detektor, der ursprünglich für die Strahldiagnose entwickelt wurde, im Hinblick auf Fluenzmessungen am Heidelberger Ionenstrahl-Therapiezentrum untersucht. Software für die Steuerung der Messung und ihre Auswertung wurde entwickelt, implementiert und genutzt, um die Auswirkungen von Kameraeinstellung, Objektiveigenschaften und der 45° Neigung des Schirms relativ zum Strahl auf das Bildsignal zu untersuchen. Darauf wurden Korrekturmethode für den Untergrund, die Vignettierung und für die Perspektive entwickelt und in Messungen des Ansprechverhaltens des Detektors angewandt. Das Signal des Detektors ist unabhängig von der Strahlintensität und zeigt eine streng lineare Abhängigkeit von der Fluenz mit einer energieabhängigen Steigung. Da die Fluenzkalibrierung große Abweichungen von Tag zu Tag zeigte, ist eine erneute Kalibrierung für jeden Messtag nötig. Ein Vergleich von gemessenen und berechneten 2D-Fluenzverteilungen aus Bestrahlungsplänen zeigte in den Messungen verbreiterte Verteilungen. Dies wird einem optischen Effekt zugeschrieben, der hier nicht korrigiert wurde und der noch weiter untersucht werden muss, bevor das System klinisch einsetzbar ist. Zusammenfassend wurde eine Methode zur Vignettierungs- und Perspektivenkorrektur entwickelt und das Detektorsystem wurde für verschiedene Strahleinstellungen charakterisiert. Schließlich wurden Anforderungen an ein optimiertes System abgeleitet.



**To my parents**  
**Ruth and Fritz Lahrmann**



# Contents

<b>1. Introduction</b>	<b>1</b>
<b>2. Materials and Methods</b>	<b>3</b>
2.1. Fundamentals . . . . .	3
2.1.1. Scanned Heavy Ion Radiotherapy . . . . .	3
2.1.2. Dosimetry of Scanned Ion Beams . . . . .	6
2.1.3. Scintillating Screens . . . . .	7
2.1.4. Aim of this Work . . . . .	8
2.2. Measurement System . . . . .	8
2.2.1. Design of the Scintillating Screen Detector . . . . .	8
2.2.1.1. Pixel Scale . . . . .	10
2.2.2. Standard Measurement Setup . . . . .	11
2.2.2.1. Determination of the Beam Isocenter . . . . .	11
2.2.3. Image Acquisition . . . . .	11
2.2.3.1. Measurement procedure . . . . .	12
2.3. Image Corrections . . . . .	13
2.3.1. Background correction . . . . .	14
2.3.2. Summation of Single-Spill Images for each iso-energy Slice . . . . .	15
2.3.3. Lens Corrections . . . . .	16
2.3.3.1. Geometrical Distortion . . . . .	16
2.3.3.2. Vignetting . . . . .	16
2.3.4. Effects of the tilted Screen . . . . .	18
2.3.4.1. Perspective Correction . . . . .	19
2.3.4.2. Intensity Correction . . . . .	21
2.3.4.3. Interpolation of the corrected Image to a regular Grid . . . . .	22
2.4. Investigation of Detector Response . . . . .	23
2.4.1. Signal Dependence on Camera Parameters . . . . .	23
2.4.1.1. Gain . . . . .	23
2.4.1.2. Aperture . . . . .	23
2.4.2. Signal Dependence on Beam Parameters . . . . .	24
2.4.2.1. Beam Intensity . . . . .	24
2.4.2.2. Particle Fluence . . . . .	24

2.4.3.	Application to Patient Treatment Plans . . . . .	24
2.4.4.	Depth-dependent Response . . . . .	25
<b>3.</b>	<b>Results</b>	<b>27</b>
3.1.	Image Scale and Corrections . . . . .	27
3.1.1.	Pixel Scale . . . . .	27
3.1.2.	Background Correction . . . . .	27
3.1.3.	Lens Corrections . . . . .	29
3.1.3.1.	Geometrical Distortion . . . . .	29
3.1.3.2.	Vignetting . . . . .	29
3.1.4.	Effects of the tilted Screen . . . . .	31
3.1.4.1.	Geometric Correction . . . . .	31
3.1.4.2.	Intensity Correction . . . . .	32
3.2.	Investigation of Detector Response . . . . .	32
3.2.1.	Signal Dependence on Camera Parameters . . . . .	33
3.2.1.1.	Gain . . . . .	33
3.2.1.2.	Aperture . . . . .	33
3.2.2.	Signal Dependence on Beam Parameters . . . . .	34
3.2.2.1.	Beam Intensity . . . . .	34
3.2.2.2.	Particle Fluence . . . . .	34
3.2.3.	Application to Patient Treatment Plans . . . . .	35
3.2.4.	Depth-dependent Response . . . . .	37
<b>4.</b>	<b>Discussion</b>	<b>41</b>
4.1.	Image Scale and Corrections . . . . .	47
4.1.1.	Pixel Scale . . . . .	48
4.1.2.	Background Correction . . . . .	48
4.1.3.	Lens Corrections . . . . .	49
4.1.3.1.	Geometrical Distortion . . . . .	49
4.1.3.2.	Vignetting . . . . .	49
4.1.4.	Effects of the tilted Screen . . . . .	50
4.2.	Investigation of Detector Response . . . . .	50
4.2.1.	Signal Dependence on Camera Parameters . . . . .	50
4.2.1.1.	Gain . . . . .	50
4.2.1.2.	Aperture . . . . .	51
4.2.2.	Signal Dependence on Beam Parameters . . . . .	51
4.2.2.1.	Beam Intensity . . . . .	51
4.2.2.2.	Particle Fluence . . . . .	51
4.2.3.	Application to Patient Treatment Plans . . . . .	51

4.2.4. Depth-dependent Response . . . . .	53
4.3. Usage of the Scintillating Screen Detector . . . . .	54
4.3.1. Fluence Measurements with the current System . . . . .	54
4.3.2. Considerations for Construction of a Scintillating Screen Detector . . .	55
<b>5. Conclusion</b>	<b>57</b>
<b>References</b>	<b>59</b>
<b>Anhang</b>	<b>63</b>
<b>A. Addendum</b>	<b>64</b>





# 1. Introduction

Current standards in modern radiotherapy demand a homogenous and highly conformal dose distribution in the target volume. With photon irradiation this is achieved using Intensity Modulated Radiation Therapy (IMRT), in which each treatment field is fluence modulated, but the fields are superimposed to form a homogenous dose distribution in the target [1].

Ion therapy represents an alternative approach to reach this goal, while offering additional advantages compared to photon therapy. The inverse depth-dose profile describes a low dose deposition in the entrance region and a sharp increase and subsequent decrease, the Bragg-peak, at the end of the particle range [2]. By modulating the energy of the ion beam, the Bragg-peak can be positioned in the tumor and steep dose gradients can be achieved at the border of the tumor to reduce the dose to the adjacent healthy tissue. Compared to photons it can also be used to escalate the dose to the tumor without increasing the dose to the surrounding areas. Additionally, the high dose ratio between peak- and entrance-region reduces the integral dose to healthy tissue.

For heavier ions (e.g. carbon ions), this effect is enhanced by special radiobiological properties. These properties are described by the Relative Biological Effectiveness (RBE), which is defined as the ratio between the photon dose and the ion dose resulting in the same biological effect [2]. The RBE depends on the Linear Energy Transfer (LET), which is defined as the ratio of the mean energy loss from collisions, in which the energy loss is below a defined value, and the travelled distance [3]. The LET and hence also the RBE is highest in the Bragg-peak enhancing the ratio of the biological effective dose between peak and entrance region.

However, a single Bragg-peak does not provide homogenous dose in the target. Therefore several Bragg-peaks are to be superimposed to compose a so-called Spread Out Bragg-Peak (SOBP). For this, two application techniques have been developed. In passive beam shaping, the beam is first scattered laterally and then a modulator wheel or a ridge filter is used to provide the spread in depth [4,5]. The position of the SOBP in depth can be controlled by adding plastic slabs in front of the beam serving as range shifter. A compensator is additionally added to adapt the distal profile of the beam to the tumour shape. However, a disadvantage of this technique is a lack of tumour conformity at the proximal part of the dose distribution.

Scanning, as an active beam shaping technique, superimposes single Bragg-peaks according to a pre-calculated 3d-pattern. Prior to treatment the tumour is virtually subdivided into iso-energy slices exhibiting the same radiological depth. Then, in lateral direction a pencil beam is controlled by steering magnets scanning the beam in a raster-like pattern and thereby covering the whole tumour cross section point by point. To reach the next iso-energy slice in a different

depth, the beam energy is adjusted and the tumour is thus irradiated slice by slice until the whole volume is covered.

Recent studies have shown the promising results of carbon ion therapy [6–12]. At the Heidelberg Ion Therapy Center (HIT), the raster scanning method is used to perform proton or carbon ion irradiations and in the future also other ion types will be applied [13, 14]. This dynamic technique requires verification of individual patient plans as well as comprehensive regular quality assurance measurements to assure correct beam delivery [15–18]. This is currently performed employing 3d ionization chamber (IC) stacks and radiographic film. As IC stacks only provide information on very few sample points and film measurements are rather time-consuming and difficult to evaluate due to their LET-dependence, additional two dimensional measurement systems with high spatial resolution are highly desirable.

As current quality assurance measurements are generally time-demanding, time efficiency has to be considered as well, when new detectors are employed and respective measurement procedures have to be developed. The importance of time effectiveness can be seen, when one considers the constant debate on cost- effectiveness of particle therapy [19–21].

Scintillating screens appear to be a suitable tool in verification and quality assurance measurements as they show a linear response to irradiation and can be combined with a CCD camera for high resolution 2d fluence measurements with digital readout, enabling effective measurement procedures. At the HIT facility, scintillating screen detectors are routinely used for beam diagnostics, however they have not been used yet to quantitatively measure fluence distributions. Aim of this work is to investigate this scintillating screen detector system for its applicability as a quality assurance tool for quantitative fluence measurements.

## 2. Materials and Methods

### 2.1. Fundamentals

#### 2.1.1. Scanned Heavy Ion Radiotherapy

For an effective radiation therapy a highly conformal dose distribution is desired in the tumor with a steep dose falloff that allows sparing of healthy tissue. A steep falloff is especially important, when a tumor lies directly adjacent to radiosensitive organs, as is for example the case for brain tumors, or when it is very radio-resistant so that the dose needs to be escalated without exposing the adjacent healthy tissue to a higher dose as well.

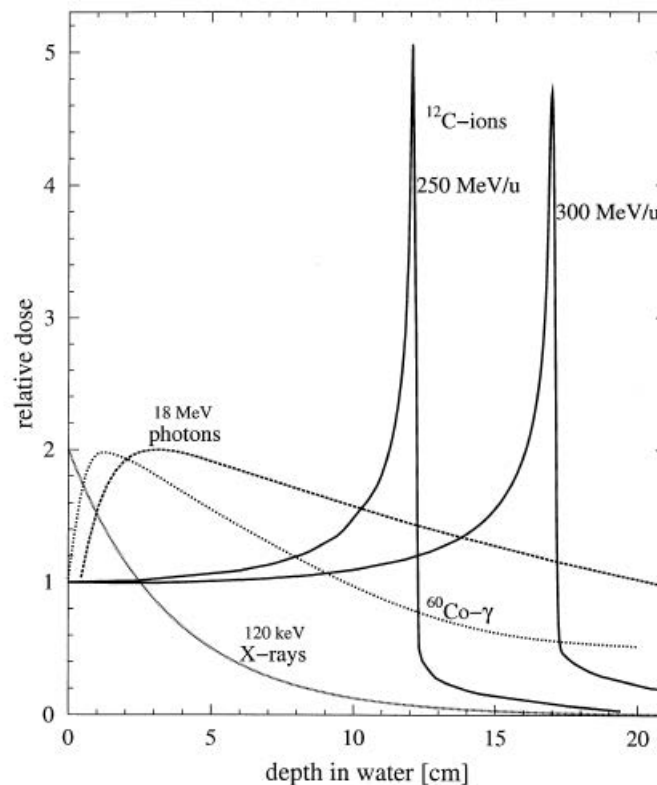


Figure 2.1.: Depth-dose curves of photons and carbon ions as illustrated in [2].

Ions interact differently with matter than photons, which leads to an inverse depth-dose profile as shown in figure 2.1. It can be seen that the dose is lowest at zero depth and increases sharply at the end of the track, where it forms the Bragg-peak and exhibits a steep falloff. In heavy

ion therapy this behavior is used to escalate the dose while sparing healthy tissue. Further, the graph shows that the depth of the Bragg-peak depends on the beam energy and therefore the beam energy is adjusted such that the peak lies in the tumor.

In scanned heavy ion radiotherapy the tumor is virtually subdivided into slices of equal water-equivalent depth, which means that the whole slice is irradiated with the same initial beam energy. Steering magnets then direct a pencil beam so that the dose is applied spot by spot in a raster pattern in this slice perpendicular to the beam. After one slice irradiated the energy is changed to irradiate the next slice until the whole 3d volume is covered (compare fig. 2.2). Scanned heavy ion therapy is subdivided into spot and raster scanning, the first referring to a technique in which the beam is switched off between single points and the second referring to a technique in which the beam is swiped to the next point without being switched off.

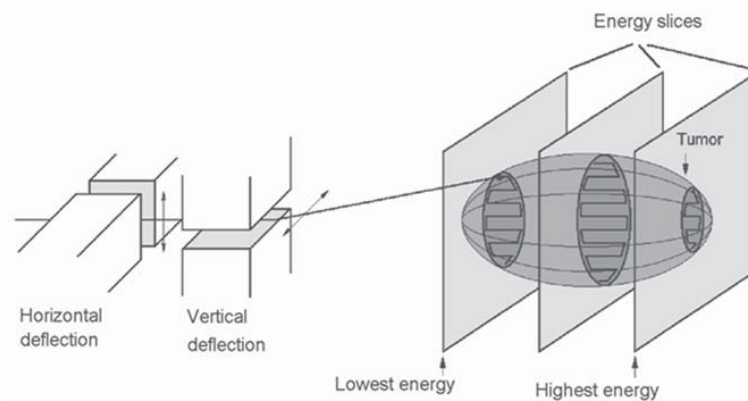


Figure 2.2.: Principle of raster scanning as illustrated in [22].

At the Heidelberg Ion-Beam Therapy Center (HIT), which is shown in figure 2.3, raster scanning is used with protons and carbon ions and experimentally also with helium and oxygen ions. Moreover, irradiation is not applied continuously, but a synchrotron provides ions spills, which last up to 5 seconds each. Therefore, one irradiation field can consist of several spills.

As this delivery technique is very complex, correct beam delivery with respect to geometry and dose has to be assured by measurements of individual patient plans as well as regular quality assurance measurements.

### *Donut Effect*

The beam monitoring system that is integrated into the beam nozzle at HIT (fig. 2.11) uses gas filled multi-wire chambers to measure the beam position. During irradiation, radiation cracking occurs causing gas molecules to break down into fragments, which then attach themselves to the chamber wires. This damage to the wires increases over time and due to the typical field sizes, the area around the isocenter is most affected. This aging effect leads to a shielding from

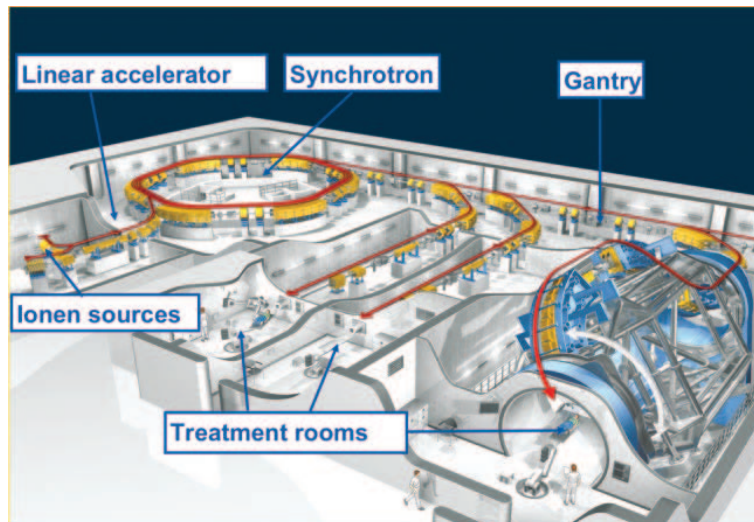


Figure 2.3.: Schematic view of the HIT facility as illustrated in [6].

the ionization cascade occurring in the chamber, which causes a slightly shifted position and width of the reconstructed beam. This information is then looped back to the treatment control unit resulting in a donut shaped area of reduced dose application around the isocenter (fig. 2.4). Due to this donut effect, the measurement chambers are replaced regularly [23].

In this work, the feedback loop between beam monitoring system and treatment control unit was disabled for the irradiation of homogenous fields to prevent the donut effect. However, for inhomogeneous fields a donut effect might occur in the evaluated images.

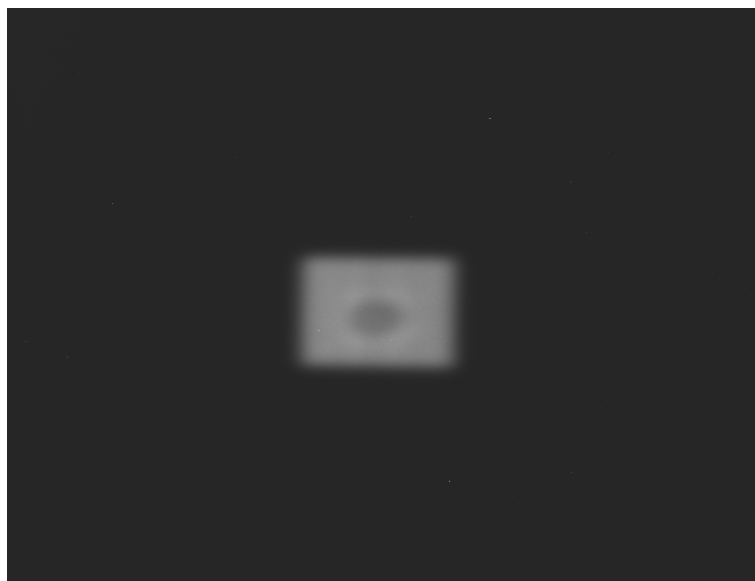


Figure 2.4.: Donut effect approximately at isocenter position.

### 2.1.2. Dosimetry of Scanned Ion Beams

As explained in 2.1.1 and in [18], in scanned ion therapy a dose distribution is build from many pencil beams with different positions and energies. As dose deviations can independently occur at any of those positions, it is not enough to compare the measured and planned dose at one position, but several positions need to be measured to obtain a sufficiently large sample.

Therefore, at HIT 3d individual patient plans are currently dosimetrically measured with a stack of ionization chambers in water (compare fig. 2.5) [24]. However, while ionization chambers are the gold-standard in dosimetry, the spatial resolution of this detector is relatively low, as the dose is measured at only 24 sample points per measurement

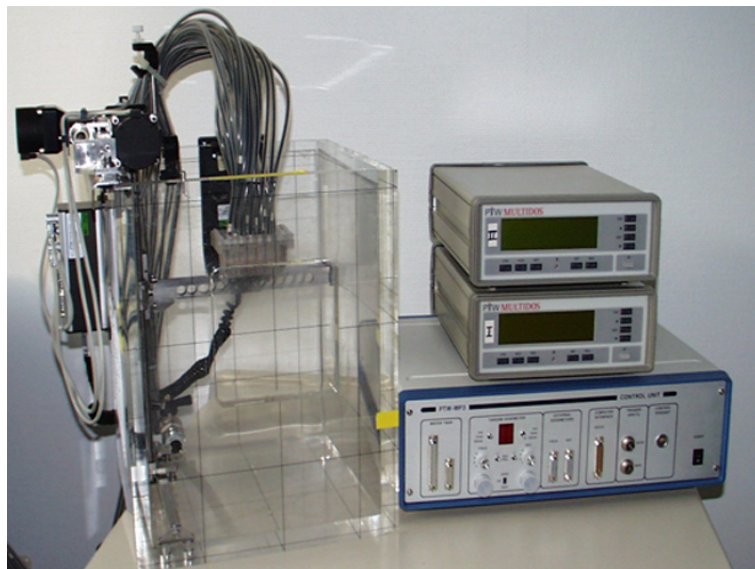


Figure 2.5.: System used for 3d dose verification: water phantom with two multidos electrometers and control computer.

2d distributions are also frequently measured in quality assurance, for example a homogeneous irradiation field is applied and measured with an array of ionization chambers to obtain the dose and additionally with radiographic film to check for instance the homogeneity of the distribution. While the film offers a 2d measurement instead of only a small sample of points, this procedure provides only limited information. Therefore, other 2d measurement options with the possibility of online-readout were investigated.

One example is the flat-panel detector RID 256 L (Perkin Elmer, Wiesbaden, Germany), based on amorphous silicon, which was investigated by Hartmann et al. [25]. The study showed that this detector has better dose-response homogeneity than the currently used radiographic film and is also sensitive to field irregularities and can therefore replace film measurements.

### 2.1.3. Scintillating Screens

To describe the basic principles of scintillators, one has to treat inorganic and organic scintillators separately [26]. Here, first inorganic scintillators are described.

Figure 2.6 shows the solid-state energy bands of an inorganic scintillating crystal. One can see the valence and the conduction band and several intermediate activator states that were introduced into the crystal through impurities. When an ionizing event occurs, an electron from the valence band is lifted into the conduction band leaving a positive charged hole. Both can migrate in their band and thus the hole can be filled with an electron from the ground state of the activator and the electron can fill an excited state, respectively. If the transition is allowed, they recombine releasing the energy difference between both states. As the energy difference between the two activator states is less than the gap between valence and conduction band, this energy is not reabsorbed and depending on the scintillator it is released in the form of visible light. However, if the transition is forbidden, the electron can be elevated by thermal energy into an activator state from which the transition is allowed and as a result light is released with a time delay. A third possibility is a radiation-less transition between activator excited and ground state, this is called quenching.

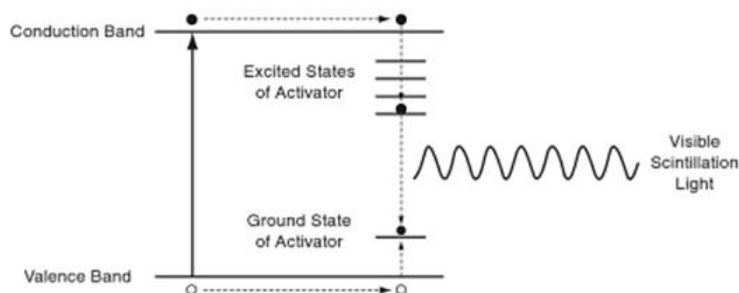


Figure 2.6.: Principle of inorganic scintillators as illustrated in [26].

In an organic scintillator no activators are added and instead the scintillation light occurs due to transitions between molecular energy levels of a single molecule. In addition, organic scintillators do not need a regular crystal lattice structure; instead they frequently show a covalent bond as in figure 2.7, in which  $S_0$  and  $S_1$  are separated by 3 eV and the vibrational states by 0,15 eV. An ionizing event excites the molecule from  $S_0$  into a higher singlet state, from which it promptly decays to  $S_1$  without photon emission. From there, it can decay back to  $S_0$  or a respective vibrational mode under fluorescence with a delay of 1ns or under phosphorescence to  $T_1$  with a delay of up to 1 ms. In practice, the organic scintillant is added to a bulk solvent, which absorbs the energy und irradiation and transfers it to the solvent.

As in both cases the excitation process depends on the deposited energy in the scintillator, the scintillation light is proportional to the dose as well. More specifically, the optical signal of the

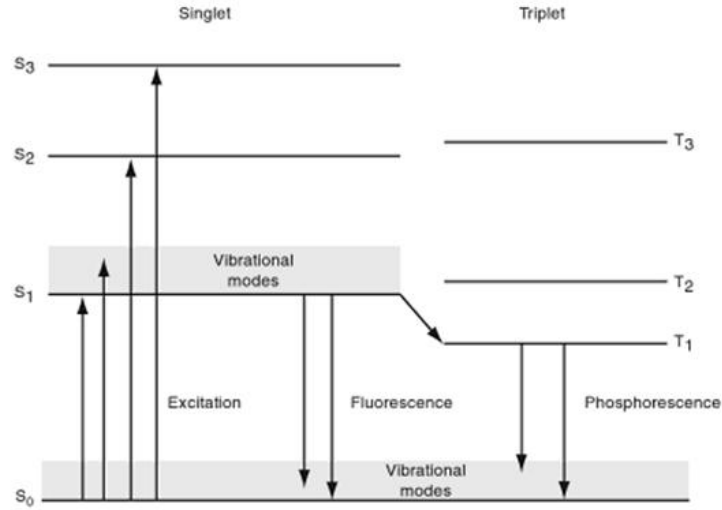


Figure 2.7.: Principle of inorganic scintillators as illustrated in [26].

scintillating screen plotted as a function of fluence is showing a linear response with the slope being proportional to the energy loss  $dE/dx$  in the scintillator.

### 2.1.4. Aim of this Work

This PhD project aims to setup a stand-alone scintillation detector system at HIT to be used for patient plan verification and quality assurance in heavy ion radiation therapy. As a result of the screen's property (compare 2.1.3), digital images of the scintillating screen can be used to verify the entrance fluence distribution at zero depth for each beam energy of a radiation field using previously measured slopes for calibration. While the camera screen system was developed before and used for tuning of the beam alignment [27], here, it shall be investigated for the first time for fluence measurements as a stand-alone system.

## 2.2. Measurement System

### 2.2.1. Design of the Scintillating Screen Detector

The setup consists of an inorganic  $Gd_2O_2S : Tb$  scintillating screen (P43 by Proxitronic, Bensheim, Germany) [28], being irradiated under a  $45^\circ$  angle, and an IEEE 1394 [29] compatible digital camera (C4742-80-12AG by Hamamatsu Photonics, Herrsching am Ammersee, Germany) [30] with a lens featuring external iris control (B2514ER by Pentax Ricoh Imaging, Hamburg, Germany) [31] mounted opposite to the screen, both enclosed with a light-tight housing (fig.2.8). The distance between camera and screen is 103 cm, the screen dimensions are  $22 \times 30 \text{ cm}^2$  and the effective size of the CCD chip is  $8.66 \times 6.60 \text{ mm}^2$ . The camera is operated



with a camera control unit, which can be connected via firewire connection to a laptop.

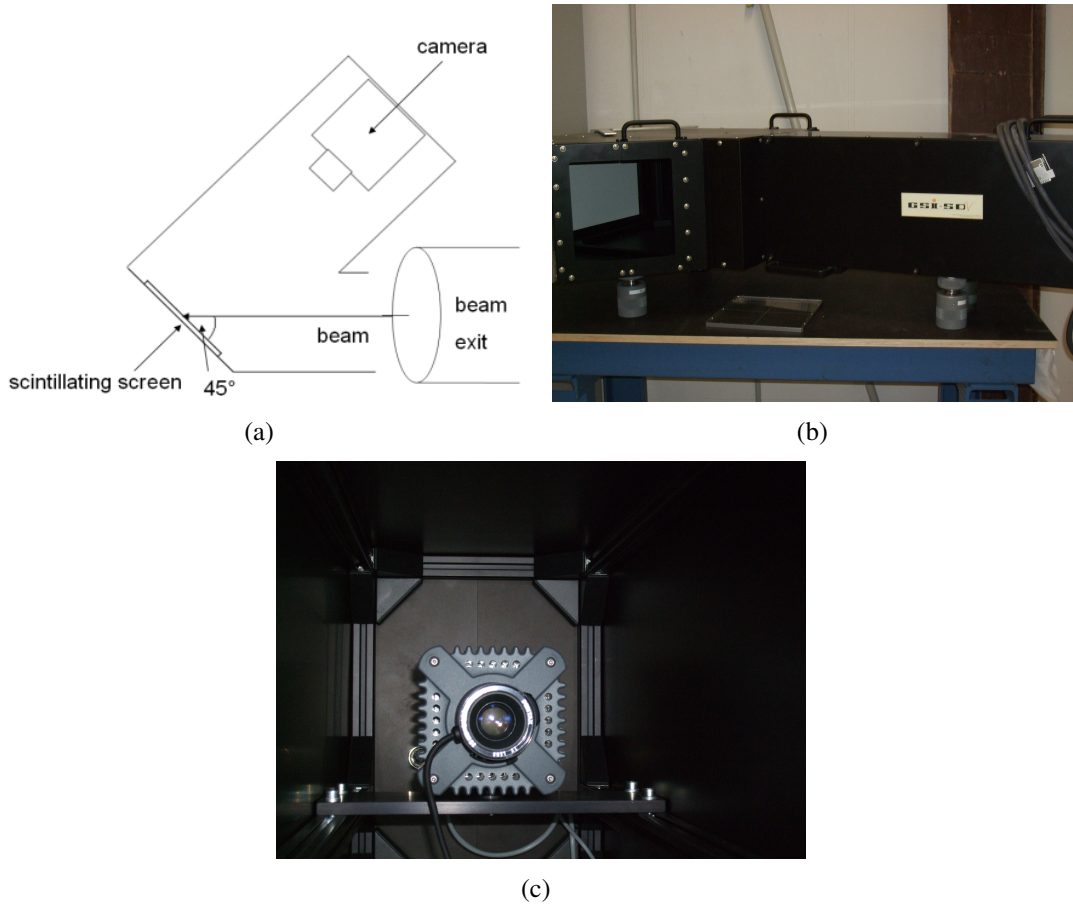


Figure 2.8.: (a) Schematic view of the scintillating screen system. (b) Front- and (c) inside-view of the detector.

Under irradiation, the scintillating screen emits visible light and the camera records this light signal in terms of grey scale images with 1344x1024 Pixels and a 12 Bit resolution. Before image acquisition, the parameters gain, exposure time and f-number of the aperture stop are adjusted. The camera gain can be configured in 256 steps from 0 dB to 20 dB (factor 1 to 10) and the camera has an electronic shutter, for which the exposure time can be chosen between 10ms - 4200s or can be determined by the length of a +5V TTL-trigger signal [30]. The aperture stop of the camera lens is controlled by a simple volt signal and can be adjusted manually in nine steps by selecting the f-number (ratio of the focal length to the effective aperture diameter) from 1.4 to "closed" (fig. 2.9). The camera possesses electronic and air cooling. Two detector systems have been used in this work. The setup of these systems is essentially the same except for the detector mounting that is adapted to the treatment room at HIT, in which the detector is to be used. In the following, these detectors are referred to as detector-E, which is the one being used at the experimental beam line and detector-H, which is used at the horizontal treatment rooms.

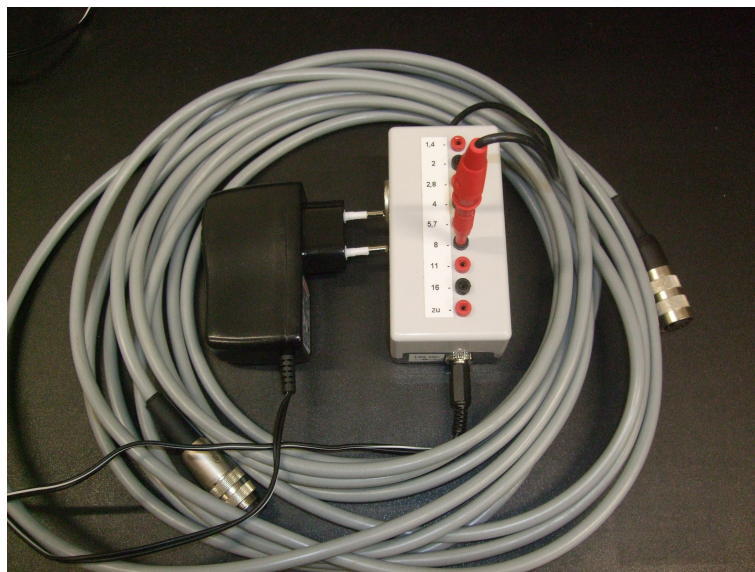


Figure 2.9.: Manual aperture stop remote control of the camera lens.

### 2.2.1.1. Pixel Scale

To measure the pixel size, the ruler placed on top of the screen was used and, additionally, millimeter paper was positioned in front of the screen (fig. 2.10). The pixel size was then averaged separately for the detector used with the experimental beam line and the one used with the horizontal treatment beam line.



Figure 2.10.: Setup to measure the pixel size.

### 2.2.2. Standard Measurement Setup

At HIT, the detector is placed on an adjustable table at the experimental beam line (fig. 2.11a) or mounted on a robotic arm in one of the horizontal treatment rooms (fig. 2.11b). In both cases, it is positioned in front of the beam nozzle with the center of the scintillating screen corresponding to the beam isocenter, which is marked in the room by lasers. The room is darkened during measurement and a black foil is taped to the entrance window of the detector to protect the measured signal from residual light sources in the room. As last part of the setup, the isocenter position on the scintillating screen is recorded (2.2.2.1).



Figure 2.11.: Measurement setup in front of the beam nozzle. (a) Detector-E at the experimental beam line. (b) Detector-H in the horizontal treatment room H2.

#### 2.2.2.1. Determination of the Beam Isocenter

The position of the beam isocenter in the image is needed to apply corrections for the tilted screen (chapter 2.3.4) and to compare the measured and planned fluence distributions. The housing of the scintillating screen system has a hatch at its rear side, where the isocenter-marking room-lasers can enter the detector when it is opened, so that an image of the laser cross can be taken with the camera (fig. 2.12).

### 2.2.3. Image Acquisition

The image acquisition software was developed in C++ and uses the CMU 1394 Digital Camera Driver [32] for camera control, the toolkit Qt [33] for the user interface and the libraries Qwt (Qt Widgets for Technical Applications) [34] and Libtiff [35] for data plotting and storing, respectively. Microsoft Visual Studio C++ 2008 Express Edition was used as the software



Figure 2.12.: Image of the room-lasers marking the isocenter.

development tool [36]. A comprehensive guide for installation of these components and integrating them into the development environment can be found in addendum A.

### 2.2.3.1. Measurement procedure

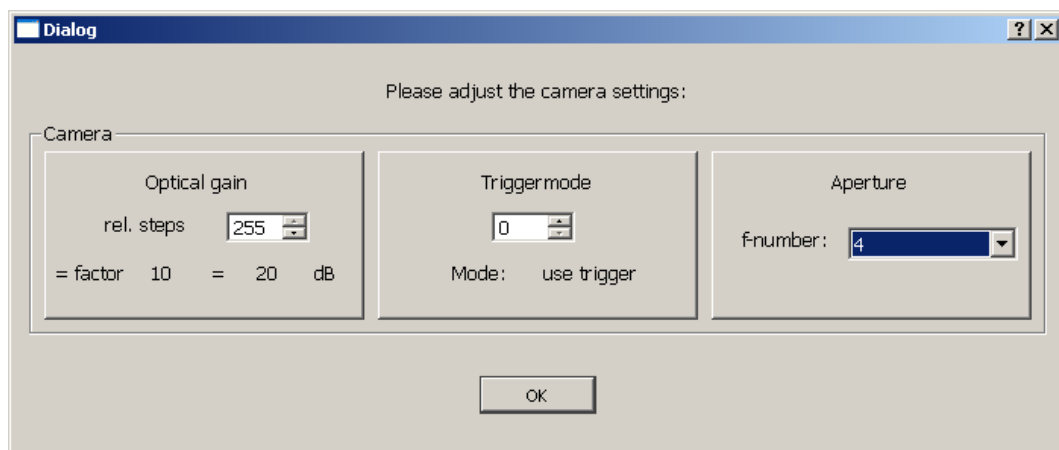


Figure 2.13.: Camera settings dialog. Gain and trigger can be adjusted here. Aperture stop has to be adjusted by hand (see fig. 2.9) and is then reported in this dialog.

For the control of the measurement procedure, a user interface was developed, which consists of two parts: the first allows remote adjustment of the camera settings (fig. 2.13) while the second controls the image acquisition process (fig. 2.14). In the following the measurement process is described:

Setting of camera gain: In the camera settings dialog (fig. 2.13), the optical gain can be set in relative steps from 0 to 255. These steps correspond linearly to approximate factors between 1 and 10. The corresponding factors and dB values are displayed in the dialog for each relative step.

Setting of trigger mode: The camera settings dialog (fig. 2.13) allows switching triggering of the camera by an external TTL-signal on or off. If the trigger is switched on, the exposure time is determined by the length of the beam on signal provided by the accelerator. If it is switched off, an exposure time of 10ms - 4200s has to be predefined in a .txt file, from which it is read during the measurement process.

Setting of Aperture: The camera settings dialog (fig. 2.13) is also used to report the f-number of the aperture stop that has to be adjusted with a manual remote (fig. 2.9) before the program is started.

Image acquisition: As stated in 2.1.1 irradiation fields can consist of several spills. Each of these spills is recorded in a separate image and those have to be recombined into complete distributions of the iso-energy slices during image processing. Recording of a new image is initialized by the rising flank of the TTL-signal and storing of the image by the descending flank. The measurement dialog displays the last two acquired images, a histogram of the number of pixel grey value and the maximum grey value in the image. This allows a direct check of the result and can be used to select the optimal camera gain.

Storage of images: The recorded 12 Bit images are stored in 16 Bit grayscale .tiff images, as this format can be viewed with standard image processing software. The camera settings during image acquisition, as well as some information on the image data (e.g. the maximum value in the image) are additionally stored in a logfile. While one image is stored per spill, only one logfile is stored per irradiated plan. This file also indicates, if connection problems between the control software and the camera occur. The name of the logfile as well as of the .tiff images contain the date and a time stamp of the measurement, the used f-number, the gain and the exposure time, if no triggering is used.

Measurement dialog providing visual output during measurement. The last two acquired images are displayed together with a histogram indicating number of pixel per grey value. In addition, the maximum grey value in the image is displayed.

## **2.3. Image Corrections**

Besides the fluence distribution, the signal of the scintillating screen is influenced by characteristics of the camera, the lens and the scintillating screen itself. Therefore, the acquired images

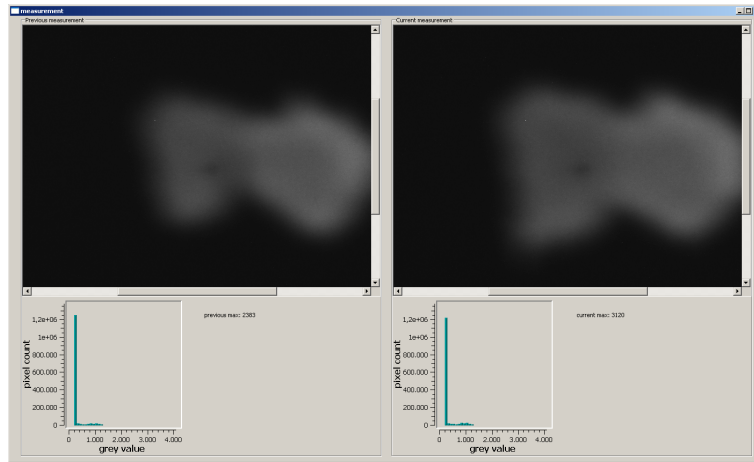


Figure 2.14.: Camera settings dialog. Gain and trigger can be adjusted here. Aperture stop has to be adjusted by hand (see fig. 2.9) and is then reported in this dialog.

have to be corrected prior to the evaluation of the fluence distribution. In the following the different corrections are described in detail (fig. 2.15):

### 2.3.1. Background correction

The acquired images are subject to white noise, which causes the camera to record a random signal in the image with a mean value of zero even when no light sources are present. As the digital image signal allows only positive values, an offset value is automatically set. As a result, the background in an image consists of an offset superimposed with positive peaks of white noise. Positive peaks in an image can also be caused by single neutrons entering the sensitive area of the camera during irradiation, which leads to nuclear interactions with constituent ions of the semiconductor lattice causing a signal in the respective sensor [37]. To remove peaks from both sources, a median filter with a radius of two is applied to all background and measurement images before further evaluation.

As the offset value might depend on the camera settings, dark images were taken for all 256 different gain values and the respective mean values, averaged over the whole image, were calculated and compared to those of a repeated measurement to check the result's reproducibility. Additionally, the homogeneity of the noise distribution in an image was investigated.

Because noise may also come from residual light from outside sources entering the housing of the scintillating screen system, the background measurements were repeated with 3 different exposure times from 1 s to 10 s and for 3 different f-numbers.

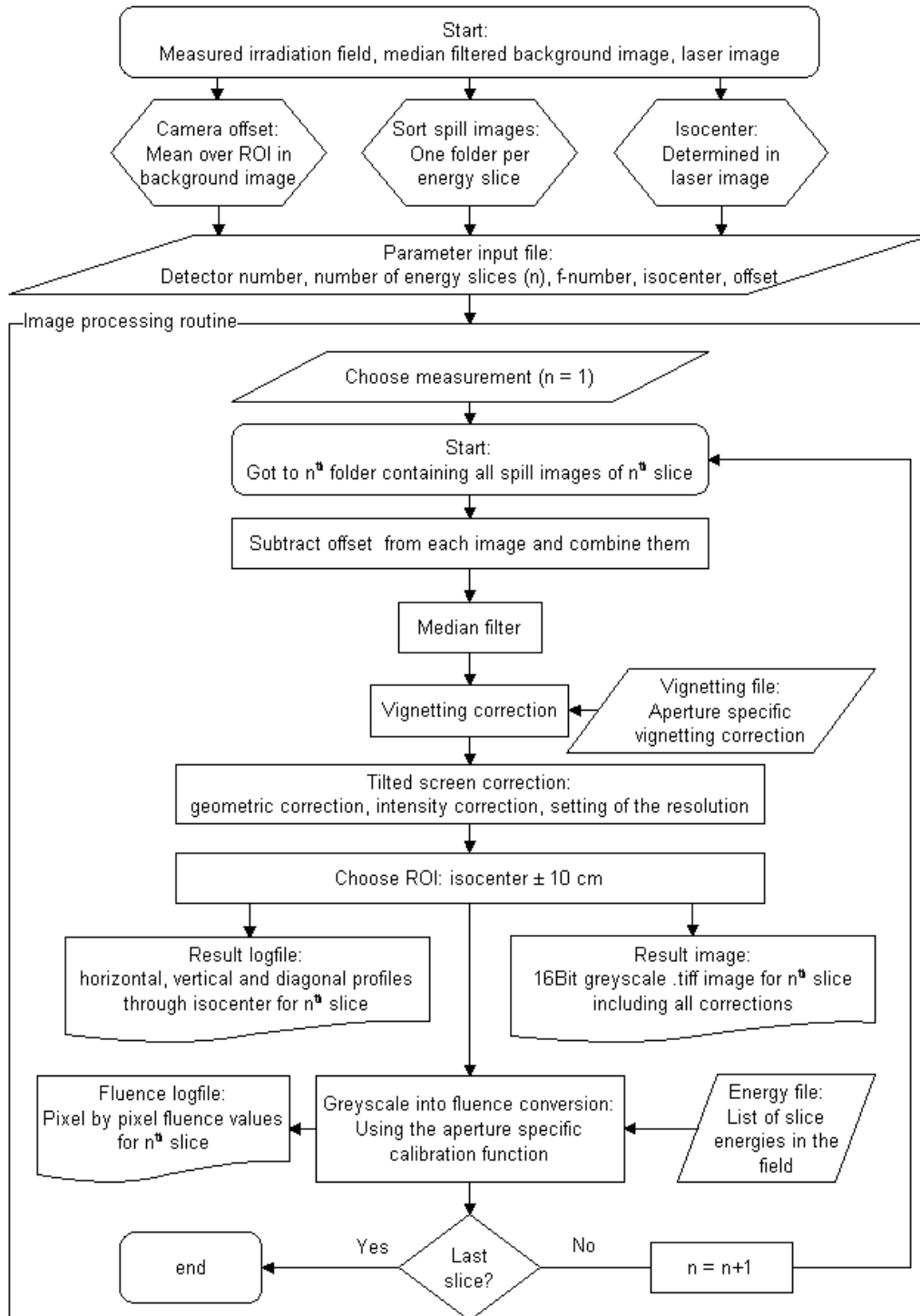


Figure 2.15.: Flowchart of the image processing.

### 2.3.2. Summation of Single-Spill Images for each iso-energy Slice

As the image acquisition was performed spill-by-spill, all background-corrected images of one iso-energy slice were summed up. As a result an image of the whole distribution in one slice is obtained (Fig. 2.16).



Figure 2.16.: Summation of spill images to irradiation fields..

### 2.3.3. Lens Corrections

To allow an absolute evaluation of the image-intensities, not only camera but also lens effects have to be corrected for. The two major effects are vignetting and geometrical distortions, which are described in the following sections.

#### 2.3.3.1. Geometrical Distortion

Presence of geometrical distortions describes a deformation of an object in the respective image. To check this for the camera-lens system, a geometrical raster was placed on the screen, similar to the setup in figure 2.10. This time, horizontal and vertical lines in the images were investigated for their straightness.

#### 2.3.3.2. Vignetting

##### *Methods to determine Vignetting*

Vignetting refers to a darkening of the peripheral part of an image. To describe the source of this effect, one has to distinguish between artificial and natural vignetting. The first primarily occurs for large aperture stops (small f-numbers) while the second can be reduced by using certain lens designs. A third type is called mechanical vignetting and describes the effect of light rays being blocked by an object that was unintentionally placed in the optical path. This type is not further discussed here.

An objective usually contains one or more lenses and apertures, which define either the part of an object that is imaged (field stop) or the light density in the image (aperture stop). Artificial vignetting occurs, when an additional aperture is inserted into the optical path causing the light density in the circular peripheral zone of the image to drop faster than without this additional aperture. Artificial vignetting may also occur, when the field stop is not placed in the object or



image plane, which results in blurry image boundaries. For cameras the field stop is equal to the film frame or the contour of the image sensor, respectively [38, 39].

Natural vignetting results from the inverse square law and Lambert's law and is proportional to  $\cos 4\phi$ , where  $\phi$  is the angle between the center of the lens and the point of interest in the object plane. The  $\cos 4\phi$  factor consists of two  $\cos 2\phi$  components. The first accounts for an increased distance between the center of the lens and the point of interest in the image by  $1/\cos \phi$  compared to the distance on the central axis. The inverse square law states a light falloff proportional to the inverse square of this distance resulting in a factor  $\cos 2\phi$ . The second component is caused by the effect that a small off axis square is not seen as a square by the lens but as a projection into the plane perpendicular to the connection line between the square and the center of the lens. Likewise, the lens is projected into this plane causing both the square and the lens to appear shortened by a factor  $\cos \phi$ . Therefore, the square emits less light into the direction of the lens according to Lambert's law and the shortened lens collects less light both resulting in the second  $\cos 2\phi$  component [40].

However, as in this work vignetting is not calculated but determined experimentally, these types of vignetting are not distinguished and instead images of a highly-homogenous light source are taken to measure the result of the combined effects for the detector specific combination of camera, lens and object-lens-distance.

#### *Establishment of a homogeneous Light Source*

A lightfoil (Slimlight by Lightec, Litzendorf, Germany) was chosen as light source. This foil consists of a semi-conductor material emitting visible light, and its specifications state an inhomogeneity of the light density of  $< 5\%$  [41]. To check the homogeneity of the emitted light distribution, an inhouse-built motorized device was employed to move a camera (EOS 5D by Canon, Krefeld, Germany) in 2 cm increments horizontally and vertically along the foil covering a  $36 \times 30 \text{ cm}^2$  area (fig. 2.11). For these measurements, the objective was enclosed in a matt dark cylinder covering the whole distance between the camera and the lightfoil to avoid stray light in the images, and the room was darkened for all measurements. To establish the respective coordinate system, a detachable cross marking the center of the foil was used for camera positioning.

Only the central  $2 \times 2 \text{ cm}^2$  of the images were later evaluated to avoid a vignetting effect in this measurement. The obtained mean values of those  $2 \times 2 \text{ cm}^2$  sections were considered to be representative for the light distribution matrix of the lightfoil and were used to correct for systematic effects on a macroscopic scale. This measurement was performed twice on two different days. Additionally, the short term (minutes) and long term (hours) time dependence of the foil's light signal was investigated for several positions.

### *Determination of the Vignetting Correction*

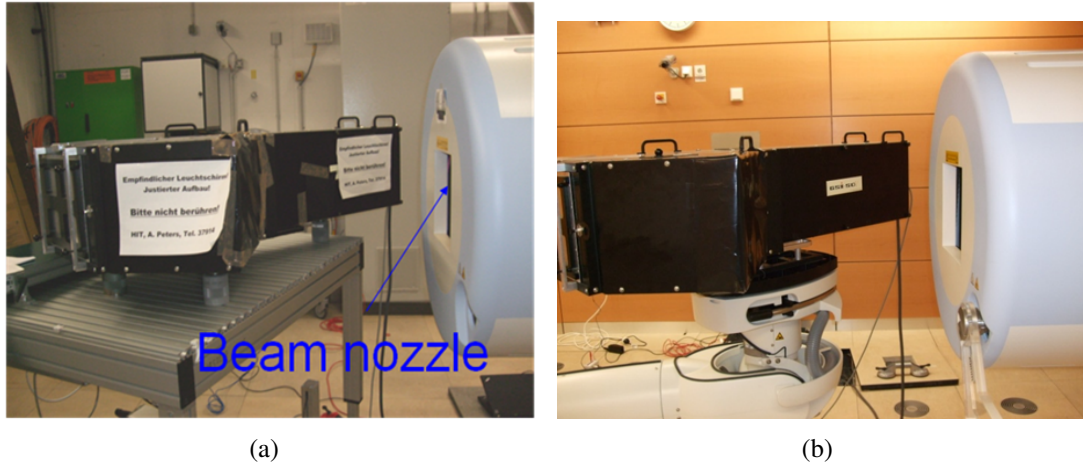


Figure 2.17.: Measurements with the lightfoil. (a) Setup to measure the homogeneity of the light density of the lightfoil. First, the camera was positioned in front of a cross that can be attached to the lightfoil to indicate the origin of the coordinate system and then, it was moved in 2 cm increments horizontally and vertically along the foil. (b) Setup to measure the vignetting correction. The camera aims at the center of the lightfoil and records an image for each lens aperture stop.

For the actual vignetting measurement the Hamamatsu camera was positioned with the central axis pointing to the origin of the coordinate system. As the cameras in the scintillating screen detectors could not be dismounted for this purpose, a camera-objective-combination identical in construction was used instead. The Hamamatsu camera was positioned in front of the center of the lightfoil by means of the detachable cross and the motorized device and the distance between the camera and the lightfoil was set to approximately the distance found in the detector (fig. 2.17). An image was then taken for each f-number.

#### **2.3.4. Effects of the tilted Screen**

As shown in figure 2.8, the scintillating screen has a  $45^\circ$  angle towards the incoming beam and is imaged by the camera with the central axis perpendicular to the center of the screen. This geometrical setup requires a perspective as well as an intensity correction, which are described in the following sections.

As shown in figure 2.8, the scintillating screen has a  $45^\circ$  angle towards the incoming beam and is imaged by the camera with the central axis perpendicular to the center of the screen. This geometrical setup requires a perspective as well as an intensity correction, which are described

in the following sections.

### 2.3.4.1. Perspective Correction

In the geometrical distortion of the image, two effects can be considered separately:

For an incoming beam that is parallel to the surface normal of the isocenter plane, the  $45^\circ$  angle would cause the image to be stretched in x direction by  $\sqrt{2}$ .

In this case, the beam has a point source leading to an additional correction depending on the distance from the irradiated point to the isocenter. Both effects result in a position dependent correction of  $\sqrt{2}$  in x direction and of a factor 1 in y direction. To derive the geometric correction, both effects are taken into account. Figure 2.18 shows the combined effect using a raster field as an example. In that case, the vertical spacing between the raster points closer to the steering magnet will be smaller than in the isocenter and those farther away from the magnet will have larger vertical spacing, respectively.

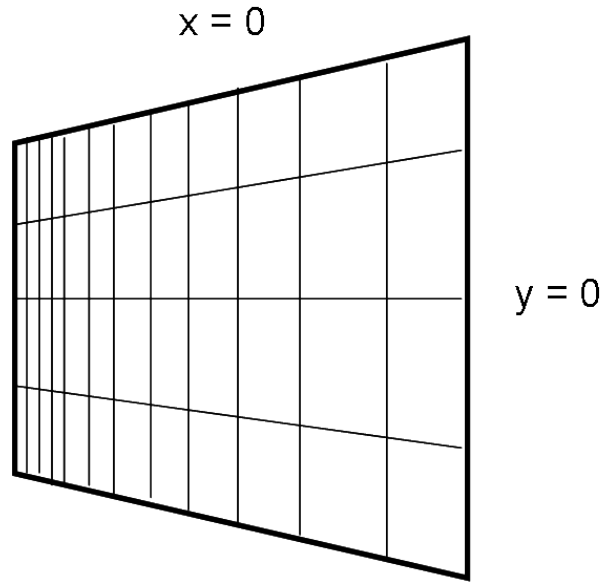


Figure 2.18.: Schematic view of the perspective correction for a raster field (not to scale).

To calculate the geometric correction due to the  $45^\circ$  angle, the scintillating screen is described as a plane in 3d space in parameter form, once as the isocenter plane E and once as a plane E' in a coordinate system tilted by  $45^\circ$  in vertical direction, and the beam is given as straight line crossing E at x.

While E is defined in a coordinate system spanned by the unit vectors  $e_x$ ,  $e_y$  and  $e_z$ , the coordinate system containing E' is spanned by these vectors:

$$e'_x = \frac{1}{\sqrt{2}}(e_x - e_z), e'_y = e_y, e'_z = e_z \quad (2.1)$$

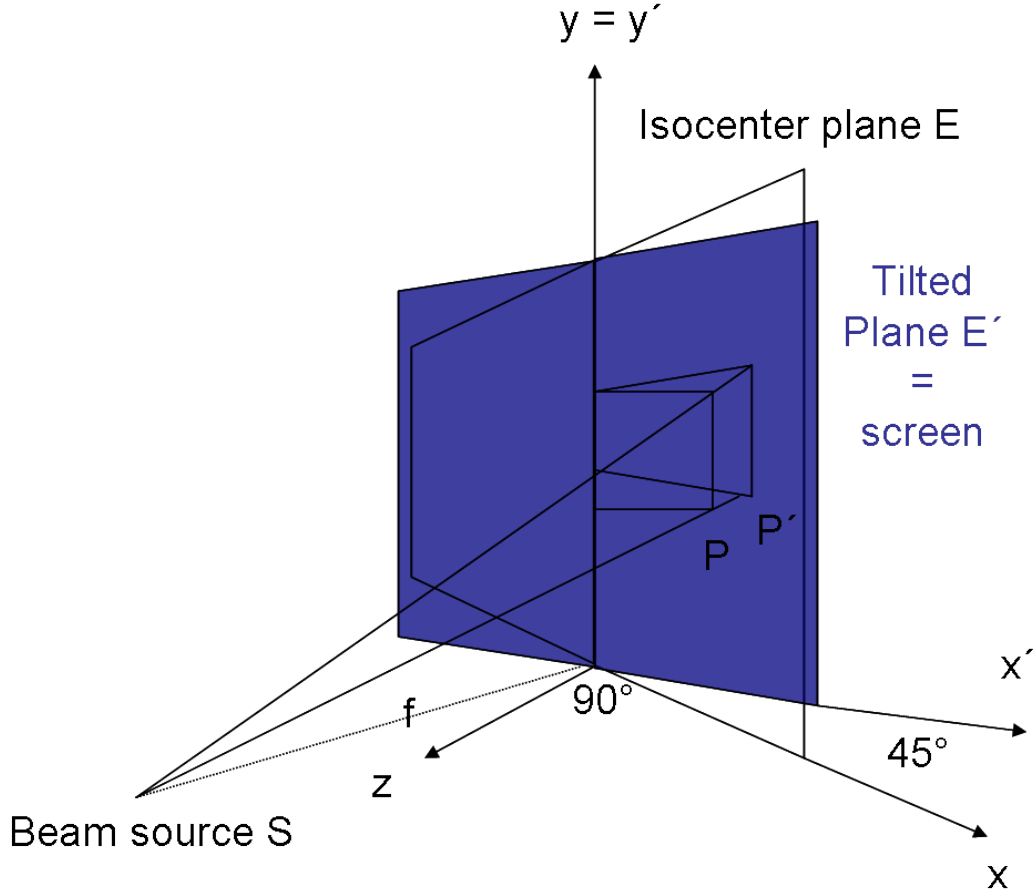


Figure 2.19.: Schematic view of the perspective correction due to the tilted screen

That leads to the following definitions:

$$E : x = ae_x + be_y \quad (2.2)$$

$$E' : x' = ge'_x + de'_y = \frac{g}{\sqrt{2}}(e_x - e_z) + de_y \quad (2.3)$$

$$g : x_g = fe_z + \epsilon(x - fe_z) = fe_z + \epsilon(ae_x + be_y - fe_z) \quad (2.4)$$

The factor  $f$  is the distance to the beam source, which equals the position of the steering magnets in the raster scan technique. Here, the distance is 6.491 m in  $x$  direction and 7.207 m in  $y$  direction, respectively. An average value was used for  $f$  in the calculation.  $E'$  can now be projected onto  $E$  by calculating the crossing point between  $g$  and  $E'$ :

$$fe_z + \epsilon(ae_x + be_y - fe_z) = \frac{g}{\sqrt{2}}(e_x - e_z) + de_y \quad (2.5)$$

Using simple algebraic manipulations and comparison of coefficients, this results in:

$$g = \frac{af\sqrt{2}}{(f-a)} \quad (2.6)$$

and

$$d = \frac{bf}{(f - a)} \quad (2.7)$$

and respectively:

$$a = \frac{f \frac{g}{\sqrt{2}}}{(f + \frac{g}{\sqrt{2}})} \quad (2.8)$$

and

$$b = d(1 - \frac{\frac{g}{\sqrt{2}}}{(f + \frac{g}{\sqrt{2}})}) \quad (2.9)$$

With these equations it is possible to describe a vector  $x = (a,b)$  in E in dependence of  $x' = (g,d)$  and therefore equations (4) can be used to map the images of the tilted screen by means of linear interpolation to the isocenter plane, which is described in 2.3.4.3. To check this method, a  $20 \times 20 \text{ cm}^2$  point raster was irradiated with the detector and with radiographic film (X-Omat V by Kodak, Stuttgart, Germany ) positioned in a plane parallel to the isocenter plane.

#### 2.3.4.2. Intensity Correction

The spatial correction described above maps the gray value of each point in the acquired image to its intersection point in the isocenter-plane without changing its signal intensity. For a parallel beam, the larger irradiated area of the tilted screen would lead to a decreased image signal, which can be described by a constant factor for the whole image and which therefore can be disregarded. In case of the HIT facility, however, we are dealing with a divergent beam. Therefore, the size of the irradiated area of the screen and hence the image intensity depends on the distance of the respective point from the source. This modified intensity has to be additionally corrected.

To calculate the intensity correction, the inverse-square law is used to derive the signal intensity  $I(P(\begin{pmatrix} x \\ y \end{pmatrix}))$  at a point of interest in the isocenter plane from its intensity  $I(P'(\begin{pmatrix} x' \\ y' \end{pmatrix}))$  in the scintillating screen plane (fig. 2.19). Here,  $\vec{x}$  denotes the distance from S to P and  $\vec{x}'$  from S to P', respectively. The inverse-square law states that the intensity of radiation, isotropically emitted by a point source, decreases quadratically with the distance to the source [3]:

$$I(P) = I(P') \left( \frac{x'^2}{x^2} \right) \quad (2.10)$$

$x$  and  $x'$  can be written as:

$$x = \begin{pmatrix} a \\ b \\ f \end{pmatrix} \quad (2.11)$$

and

$$x' = \begin{pmatrix} g \\ d \\ f + f' \end{pmatrix} \quad (2.12)$$

with  $f'$  denoting the distance between P and P'. That can be inserted into (5), leading to:

$$I(P) = I(P')(g^2 + d^2 + (f + f')^2)/(a^2 + b^2 + f^2) \quad (2.13)$$

The factor between  $I(P)$  and  $I(P')$  in equation (7) is the intensity correction factor. All variables in this factor are known and can be calculated in cm except for  $f'$ . To find  $f'$ ,  $x'$  is written in coordinate system E according to equation (2):

$$x' = \begin{pmatrix} \frac{g}{\sqrt{2}} \\ d \\ \frac{-g}{\sqrt{2}} \end{pmatrix} \quad (2.14)$$

$f'$  is therefore:

$$f' = \sqrt{(a - \frac{g}{\sqrt{2}})^2 + (b - d)^2 + (0 - \frac{g}{\sqrt{2}})^2} \quad (2.15)$$

The multiplicative correction factor in (7) is used, when the measured coordinates are mapped to the isocenter as described in 2.3.4.1. To check the intensity correction, homogenous  $20 \times 20 \text{ cm}^2$  and  $5 \times 5 \text{ cm}^2$  fields were irradiated again using the detector and radiographic film (X-Omat V by Kodak, Stuttgart, Germany) positioned in a plane parallel to the isocenter plane.

### 2.3.4.3. Interpolation of the corrected Image to a regular Grid

When the perspective correction is applied, a rectangular distorted image is converted into an image with a regular grid. At the same time the pixel scale is adapted from 38 Pixel/cm for Detector-E and 37 Pixel/cm for Detector-H, respectively, to a scale of 25 Pixel/cm, which is also used in the calculation of fluence distributions from treatment plans, and hence facilitates the comparison between measured and calculated distributions. The new image size is then  $512 \times 512$  Pixel.

For the conversion, each of the pixel positions in the new image is first converted to a cm position and with these coordinates, the corresponding position in the measured image is found taking the perspective correction into account (fig. 2.20). The measured image value at that position is multiplied with the intensity correction factor and stored in the new image. However, as the corresponding position in the measured image can typically not be found at an exact pixel position, the image value at that position is interpolated from the four nearest pixels as shown

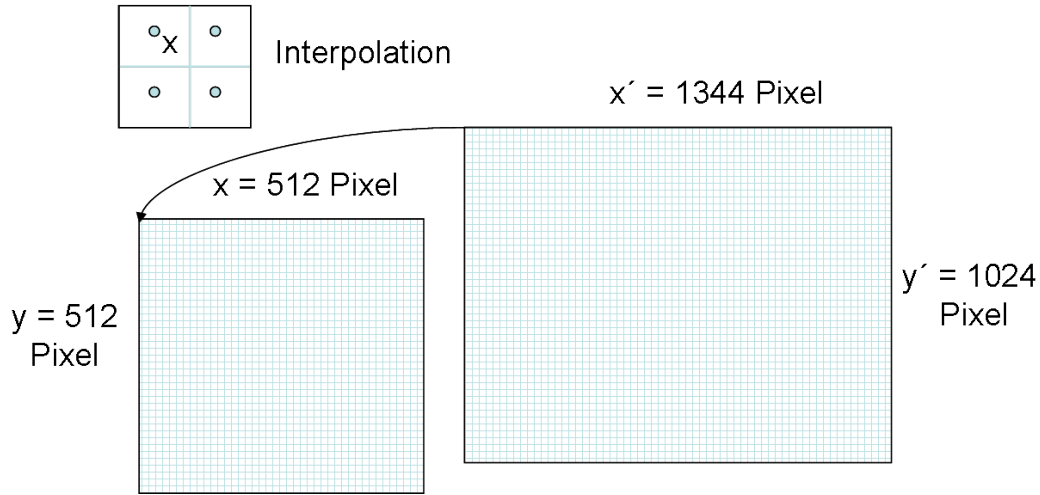


Figure 2.20.: Schematic view of the interpolation from the tilted screen to the isocenter plane.

in figure 2.20.

## 2.4. Investigation of Detector Response

### 2.4.1. Signal Dependence on Camera Parameters

As initial measurements, the signal dependence on gain and f-number was checked.

#### 2.4.1.1. Gain

To investigate the signal dependence on gain, a  $5 \times 5 \text{ cm}^2$  field was repeatedly irradiated and recorded with different gain settings, using the same f-number and the same beam parameters. This measurement was done twice on different days and with different fluences, once focusing on low and once on high gain factors. A linear dependence of the signal on gain is expected.

#### 2.4.1.2. Aperture

To test the signal dependence on the f-number, again, a  $5 \times 5 \text{ cm}^2$  field was repeatedly irradiated and the f-number was changed for each measurement, while keeping other camera and beam parameters constant. To keep the gain factor constant and considering the limited dynamic range of the detector, the measurement had to be split into two parts with different fluences, each covering four f-numbers. The signal is expected to decrease with  $\frac{1}{f^2}$  [38].

### 2.4.2. Signal Dependence on Beam Parameters

To characterize the radiation response, the dependence of the signal on Flux (particles/s) and Fluence (particles/cm<sup>2</sup>) was investigated. The latter is subsequently used for a fluence calibration.

#### 2.4.2.1. Beam Intensity

At HIT, 8 different intensity levels can be chosen for carbon ion irradiation, ranging from a particle flux of  $5 * 10^6 \text{ ions/s}$  to  $8 * 10^7 \text{ ions/s}$ . As for the investigation of camera parameters, a  $5 \times 5 \text{ cm}^2$  field was repeatedly irradiated with the same particle fluence and camera parameters, but with different particle flux. Two sets of measurement were acquired with different fixed particle fluences and gains adjusting the measurement signal to 80%. No intensity dependence is expected.

#### 2.4.2.2. Particle Fluence

The scintillation light signal is proportional to the beam fluence with an energy-dependent constant of proportionality (with  $S_{d=0}$  being the signal at zero depth):

$$S_{d=0} = m(E) * \phi \quad (2.16)$$

Therefore, a fluence calibration can be performed by recording the signal-dependence on fluence for different energies. The obtained energy dependent calibration curves can then be used to fit a function to the data that describes the energy-dependent slope  $m(E)$ . This function is needed to convert a light signal distribution resulting from a measurement into a fluence distribution.

Here, the signal dependence on beam fluence was measured for 9 beam energies from 89 MeV/u to 430 MeV/u. For each energy, a  $5 \times 5 \text{ cm}^2$  field was irradiated several times with fluences from  $6.25 * 10^5 \text{ ions/cm}^2$  to  $1.6 * 10^8 \text{ ions/cm}^2$  and measured with the same camera parameters and beam intensities. This measurement series was performed for the two f-numbers that are used most frequently.

### 2.4.3. Application to Patient Treatment Plans

To test, whether the corrected detector images can be used to determine the fluence distribution in quality assurance measurements, four treatment plans from patients were measured with the detector and the reconstructed fluence distribution was compared with that calculated from the



treatment plan. Using the machine steering file and the treatment planning system TRiP, the 2D-dose distribution was calculated at a water-equivalent depth of 0 mm at the position of the isocenter. This dose distribution was then converted to fluence distributions by means of the respective stopping powers used in treatment planning. Before each measurement, the suitable gain step was determined by irradiating the detector with the parts of the irradiation plan containing the highest fluences.

#### **2.4.4. Depth-dependent Response**

To investigate the signal response on LET an adjustable water column [42] (fig. 2.19) was used for depth modulation, while the detector was irradiated with single spots of 4 different beam energies (using the same camera and beam parameters otherwise) to scan the respective Bragg peak and thereby the high-LET area. The water column is mounted on wheels and its length axis was manually aligned with the beam axis. It was positioned as close as possible to the detector entrance to minimize the scattering distance between column and scintillating screen. For this purpose, as a modification of the standard measurement setup, the distance between scintillating screen and beam exit had to be increased to make room for the column. It can be controlled from outside the treatment room and the control software allows setting directly the desired thickness, which is then automatically applied to the water column. That way, it can be adjusted with  $\mu\text{m}$  precision with a minimum water equivalent thickness of 3.71 cm. Before the measurement, the gain was adapted to reach a signal of 80% at the minimum thickness of the water column. The resulting Bragg curves are compared to the Bragg-Curves used for treatment planning at HIT.

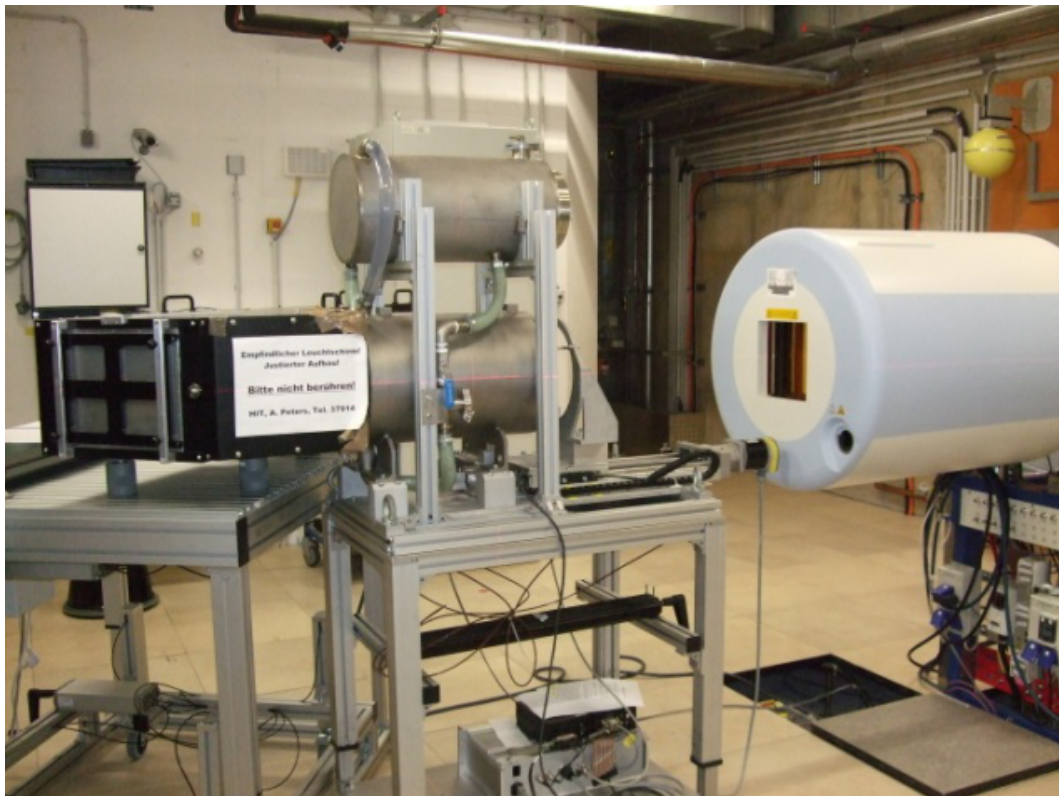


Figure 2.21.: Setup to measure the depth-dependent response of the scintillating screen system. An adjustable water column is positioned as close as possible in front of the detector.

## 3. Results

### 3.1. Image Scale and Corrections

This section summarizes the investigation of the main factors influencing the measurement and the determination of respective corrections that will be applied to all images before they are evaluated.

#### 3.1.1. Pixel Scale

For both detectors, the image with the best illumination was chosen to determine the conversion from pixel to mm from line segments, as long as possible, on the integrated ruler as well as horizontally and vertically on the attached millimeter paper. Averaging over these values, resulted in a pixel scale of  $0.2614 \pm 0.0009 \text{ mm/pixel}$ , corresponding to  $38.3 \pm 0.1 \text{ pixel/cm}$ , for Detector-E (fig. 2.2a) and of  $0.2698 \pm 0.0008 \text{ mm/pixel}$ , corresponding to  $37.1 \pm 0.1 \text{ pixel/cm}$ , for Detector-H (fig. 2.2b).

#### 3.1.2. Background Correction

Figure 3.1(a) displays a 12 Bit background measurement that consists of an offset gray value of 201 and random positive peaks with a gray value up to 500 as described earlier in 2.3.1. Single peaks lower than the offset value can also be observed. The graph (b) in 3.1 shows the result of an applied median filter with a two pixel radius, removing the peaks from the image and leaving only the background offset.

A similar pattern can be observed in the background of irradiated fields as can be seen in figure 3.1 (c) . Here, additionally to the background peaks, one finds line and cluster patterns caused by neutron interactions with the camera chip. Examples for this background contribution are marked as 1 and 2. The image (d) in 3.1 shows again that a median filter with a two pixel radius removes the peaks almost completely. Therefore, a median filter with a radius of two was applied for all raw-images in this work, if not stated otherwise. A time-efficient median filter method according to Numerical Recipes [43] was used.

Figure 3.2 contains further investigations of the offset value after application of the median filter. The result of a comparison of the mean background values for gain steps from 0 to 255, measured on two different days, is displayed in figure 3.2a. The plot shows a decreasing offset value for increasing gain. It can also be seen that the mean values measured on different days differ by more than one standard deviation from each other with an increasing deviation for

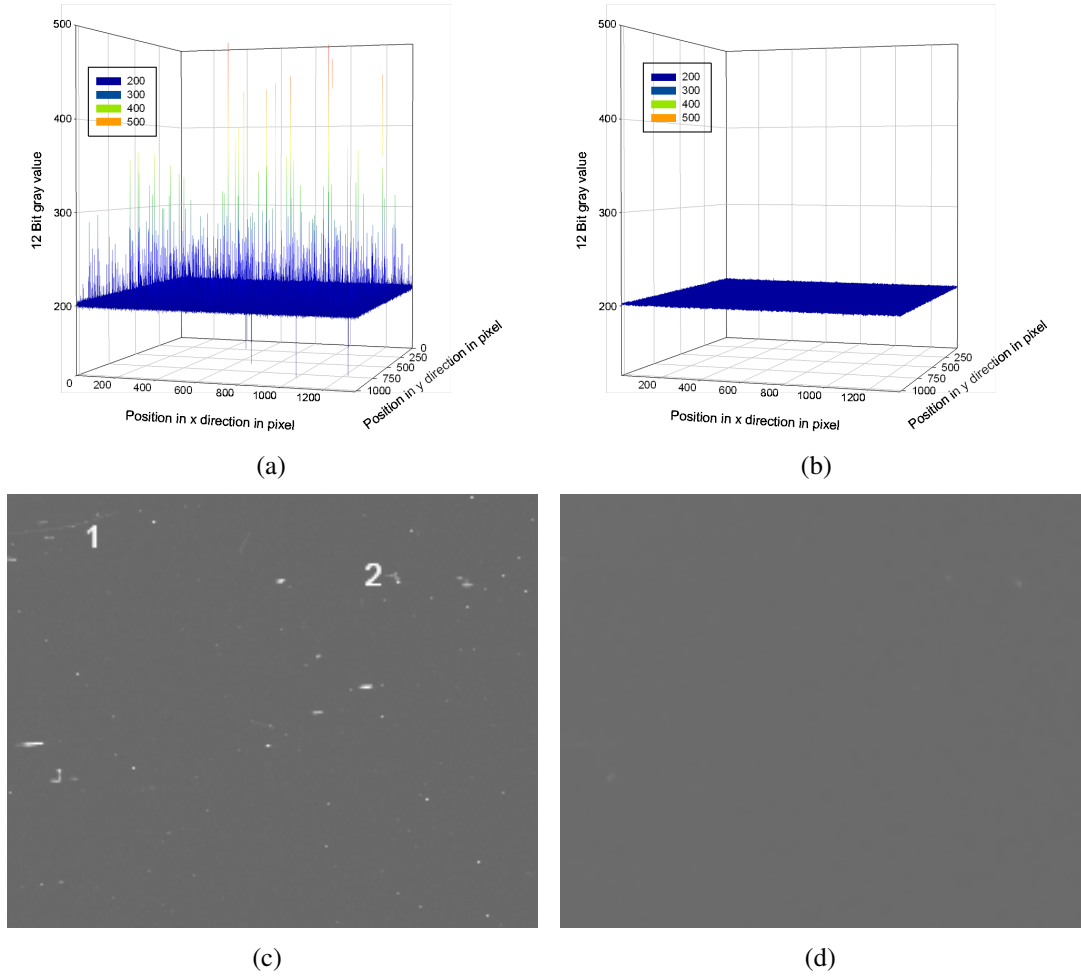


Figure 3.1.: Peaks in the background signal before and after application of a median filter (radius = 2). (a) and (b) Background signal without irradiation (gain 0). (c) and (d) Enlarged section of the background signal in an irradiated image consisting of several spills (gain 0). Brightness and contrast were enhanced to improve visibility of the displayed image.

higher gain steps. However, the mean values on both days follow the same decreasing pattern. The homogeneity of the residual 2d background distribution after filtering was investigated as well and figure 3.2b shows an example for a measurement with the highest gain. The blue lines indicate the area of the screen that can be irradiated, considering the maximum  $20 \times 20 \text{ cm}^2$  field size, and inside these boundaries a uniform distribution could be observed for all investigated background images.

To ascertain, whether part of the background is caused by residual light from outside sources, the background was measured for different exposure times and different apertures shown in figure 3.2c and 3.2d, respectively. Neither of these measurements indicates a significant difference for a longer exposure or a smaller f-number.

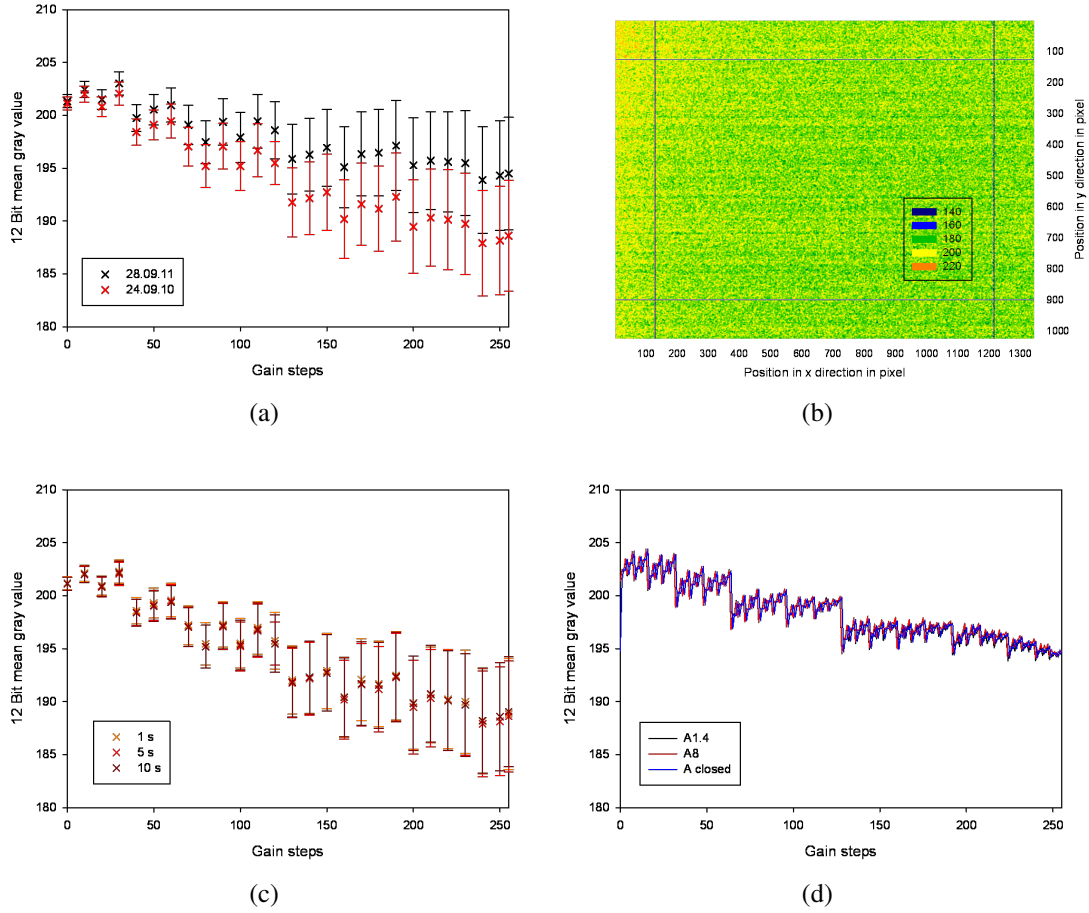


Figure 3.2.: Investigation of the median filtered image signal without irradiation. (a) Comparison of measurements on two different days. (b) Two-dimensional 12 bit gray value signal distribution for maximum gain. Reference lines indicate the boundaries the 20\*20 cm<sup>2</sup> area that can be irradiated. (c) Comparison of the background for three different exposure times. (d) Comparison of the background between three different f-numbers and for all available 256 gain steps.

### 3.1.3. Lens Corrections

#### 3.1.3.1. Geometrical Distortion

An evaluation of single lines in images of millimeter paper resulted in a distortion effect of up to 1 pixel in horizontal (28 cm) and vertical (18 cm) direction, which corresponds to a geometrical error of  $\leq 0.15\%$ .

#### 3.1.3.2. Vignetting

##### *Establishment of a homogeneous Light Source*

As a very homogenous light source is needed to quantify vignetting, the lightfoil that was chosen as source was scanned in 2 cm steps as described in section 2.3.3.2 and figure 3.3a shows the resulting 16 Bit distribution of the light signal averaged over the 4 cm<sup>2</sup> regions. While only a

### 3. Results

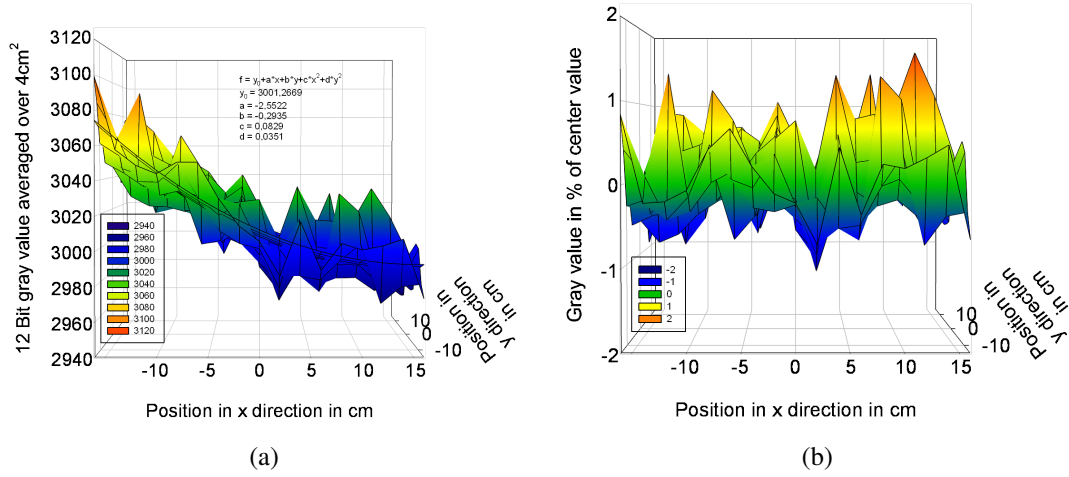


Figure 3.3.: Light density distribution of the lightfoil. (a) Original distribution with two-dimensional regression function. (b) Residual distribution after correction of the systematic decrease.

marginal signal dependence of the light intensity in y direction was found, a systematic decrease of approximately 3% was found in x direction. To correct for this systematic behaviour, this distribution was fitted with a 2d paraboloid function using a weighted least square algorithm. The residual light density distribution of the foil, normalized to the central value, is plotted in figure 3.3 . The difference between maximum and minimum light signal of the foil was thereby reduced to 2.8%.

#### *Determination of the Vignetting Correction*

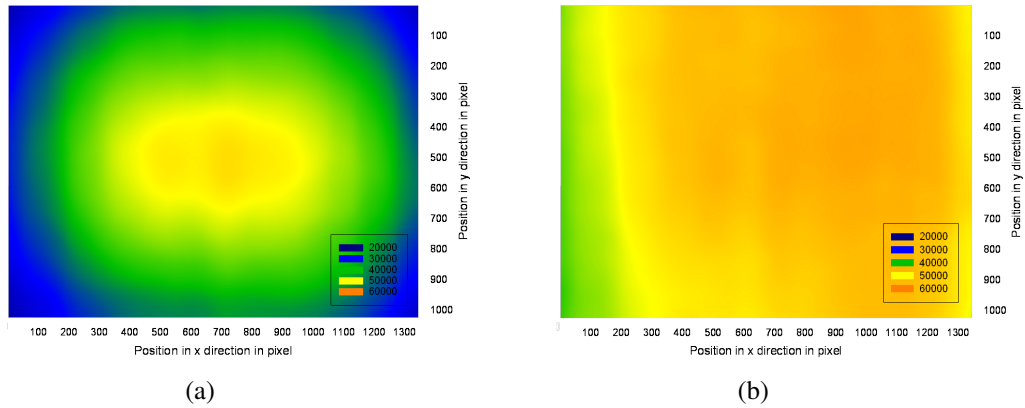


Figure 3.4.: Two-dimensional median filtered (radius = 100) vignetting distribution for two aperture stops. (a) F-number 1.4. (b) F-number 8.

To determine the vignetting distribution, images of the lightfoil were taken for all f-numbers in two independent measurement sessions. For each measurement the inhomogeneity of the light foil was corrected by using the above polynomial function. Figure 3.4 shows exemplarily the 2d result of one of those measurements for a small and medium f-number. For figure 3.5 the mean value between both measurements of each f-number was taken for each pixel and the diagonal profiles were displayed. It was observed that both measurements show good agreement

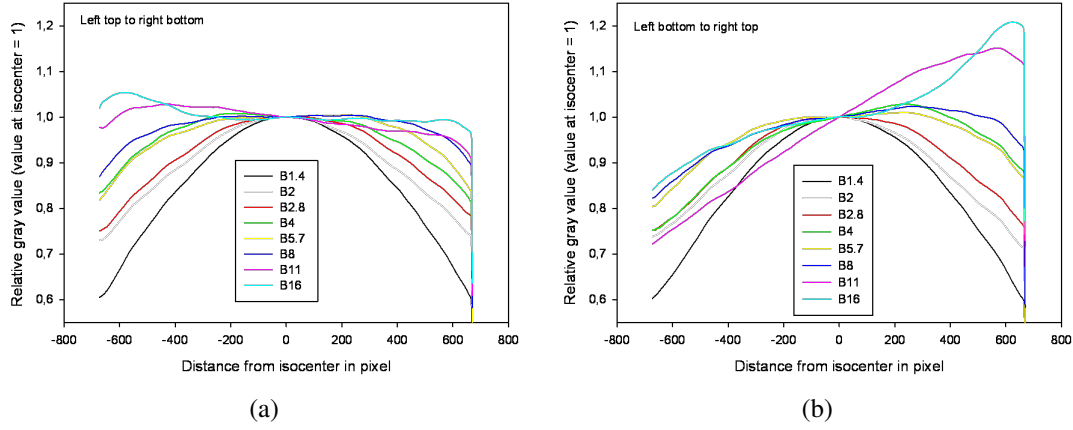


Figure 3.5.: Diagonal profiles of the median filtered (radius = 100) two-dimensional vignetting distribution for 8 aperture stops, each averaged over two measurements.

with deviations of up to 1.4% from the mean value in the  $5 \times 5 \text{ cm}^2$  center region and deviations of up to 3.0% for higher f-numbers in the outer region of a  $20 \times 20 \text{ cm}^2$  field. In figure 3.5 one can also see that for small f-numbers of the lens, a symmetric vignetting correction was found, while for higher values a significant asymmetric behavior was observed. Figure 3.4 supports this observation.

### 3.1.4. Effects of the tilted Screen

#### 3.1.4.1. Geometric Correction

To check the calculated geometrical correction for the  $45^\circ$  angle between incoming beam and scintillating screen (compare figure 2.1), a point raster was irradiated and measured with the scintillating screen detector and, additionally, with radiographic film positioned perpendicular to the incoming beam. The raster positions were in both cases determined by the center of gravity of the respective raster point. Due to the detector setup, the film could not be placed in the isocenter plane, so as a first evaluation step, the raster positions were projected to the isocenter. In figure 3.6 the raster positions on the film projected to the isocenter plane are used as the gold-standard and are compared to the positions resulting from the scintillating screen detector measurement. The red crosses in figure 3.6a represent the raster positions measured with the scintillating screen, after their horizontal distance to the isocenter was scaled by . It can be seen that the distance between the raster points in x and y direction increases with increasing x values. In figure 3.6b , showing the result after application of the geometric correction, this behavior is much less pronounced. The residual distance between the gold-standard and the scintillating screen measurement is summarized in a histogram in figure 3.7 . The mean residual distance is less than  $0.2 \text{ mm}$  in both directions.

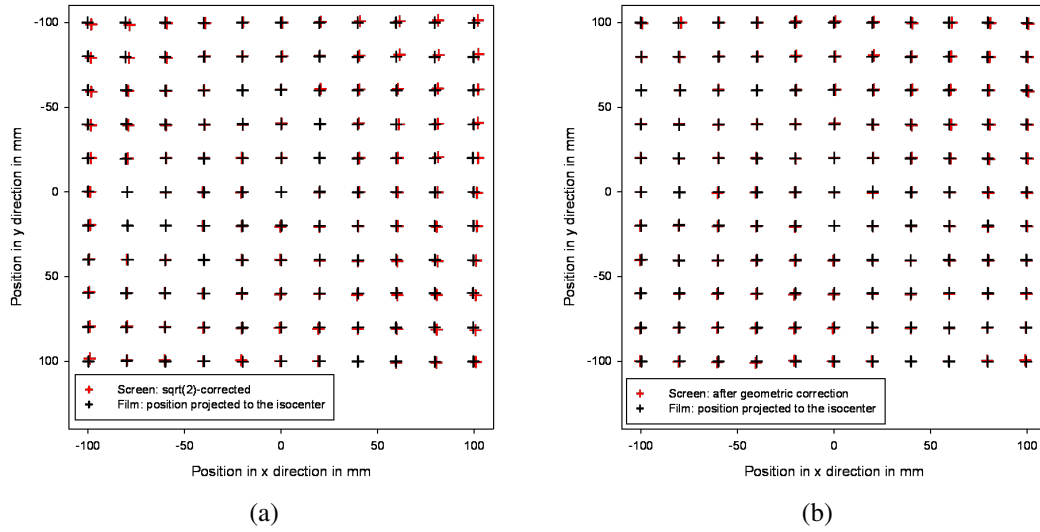


Figure 3.6.: Comparison of raster positions on film (projected to the isocenter) and on the scintillating screen. (a) Before geometric correction of the raster positions on screen. For better comparability, with the film image, the horizontal positions were scaled by  $\sqrt{2}$ . (b) After geometric correction of the raster positions on screen.

#### 3.1.4.2. Intensity Correction

As the intensity correction is more pronounced for larger distances from the isocenter, two identical homogenous  $5 \times 5 \text{ cm}^2$  fields, shown in figure 3.8a, were irradiated close to the boundary of the field of view of the accelerator to check the calculated intensity correction. As both fields were irradiated with the same fluence, the same gray value is expected. Figure 3.8b compares profile values for both fields before and after geometric correction was applied. One can see that on the left side, where the distance between beam source and screen is shortest, the signal is higher than on the right side, which is farther away from the source. After geometric correction is applied, both profiles average at the same gray value.

## 3.2. Investigation of Detector Response

This section shows initial measurements to check the signal dependence on camera parameters and beam intensity. Then, the results of the fluence calibration measurements are reported and applied to the measurement of patient irradiation plans. Additionally, an investigation of depth-dependent response of the detector is presented.



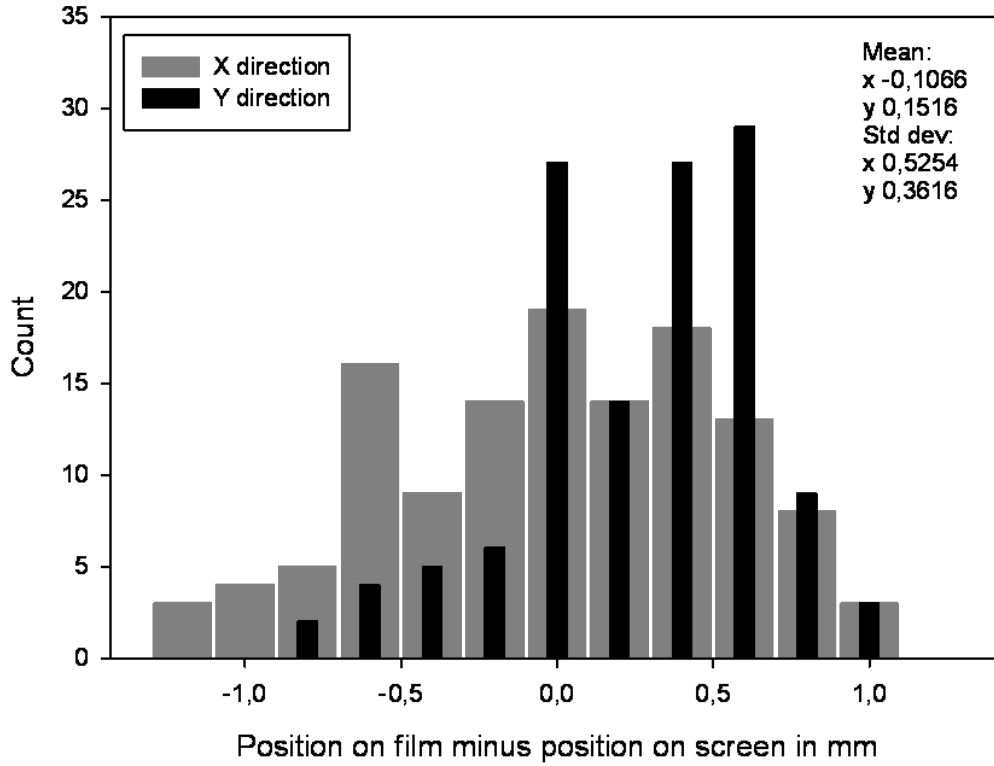


Figure 3.7.: Residual distance between raster positions on film (projected to the isocenter) and on screen after geometric correction.

### 3.2.1. Signal Dependence on Camera Parameters

#### 3.2.1.1. Gain

As shown in figure 3.9 the dependence of the mean gray value of a  $5 \times 5 \text{ cm}^2$  field on gain was investigated in two measurements on different days and with different fluences. When only the results for gain zero are compared and the result in the left graph is used as calibration, it can be noted that the signal value in the right graph is 31% higher than expected. To compare all values in both measurements, each was divided by the signal obtained with gain step 0, which is plotted in figure 3.10. This normalization divided the combined measurement into two segments with linear dependence between signal and gain, one for gain steps up to 120 and one for gain step 128 and higher. A separate weighted linear regression of these two segments lead to similar slopes of  $(3.50 \pm 0.03) \cdot 10^{-2}$  and  $(3.75 \pm 0.03) \cdot 10^{-2}$  with different y-intercepts of  $2.193 \pm 0.052$  and  $0.993 \pm 0.009$ .

#### 3.2.1.2. Aperture

Figure 3.11 summarizes the behavior of the measured signal for increasing f-numbers in comparison to the theoretical  $1/f^2$  decrease. The curve on the left is normalized at  $f = 1.4$  and the

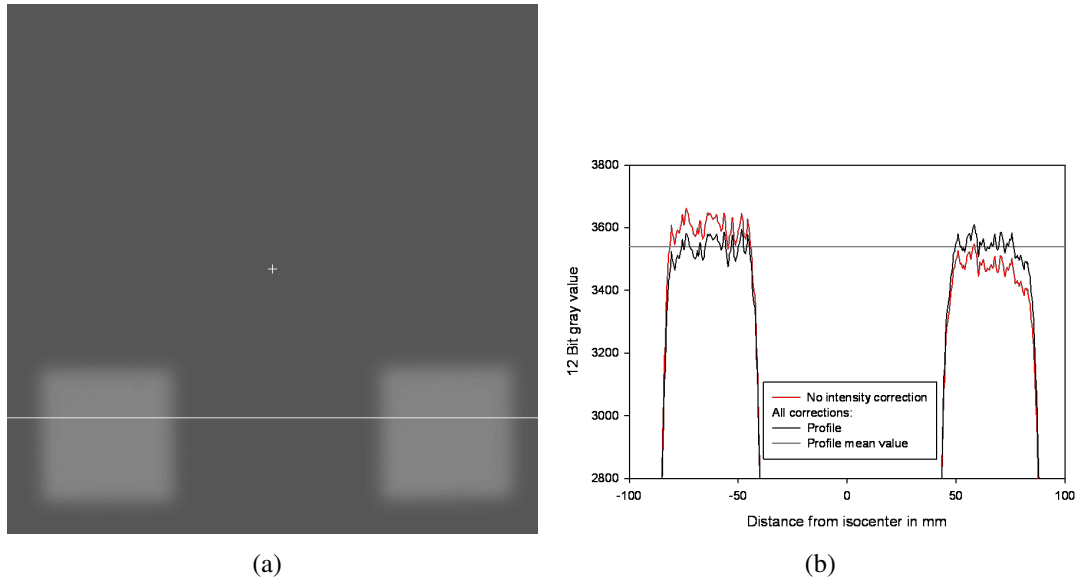


Figure 3.8.: Verification of the calculated intensity correction due to a  $45^\circ$  angle between the incoming beam and the scintillating screen. (a) Completely corrected image of two homogenous  $5 \times 5 \text{ cm}^2$  fields placed close to the boundary of the  $20 \times 20 \text{ cm}^2$  area that can be irradiated. The horizontal line marks the profile and the cross shows the isocenter position. Brightness and contrast were enhanced to improve visibility of the displayed image. (b) Horizontal profile of the geometrically corrected image with and without intensity correction.

left curve at  $f = 5.7$ , respectively. In both graphs the measured decrease exceeds the theoretical decrease.

### 3.2.2. Signal Dependence on Beam Parameters

#### 3.2.2.1. Beam Intensity

Two measurement-sets recording the mean gray value of a  $5 \times 5 \text{ cm}^2$  field for different particle flux settings are displayed in figure 3.12 and show no dependence between the detector signal and the beam intensity setting.

#### 3.2.2.2. Particle Fluence

The fluence calibration was performed with 9 beam energies for the f-numbers 4 (see figure 3.13 a and b ) and 8. The measurement with f-number 8 was performed twice on separate days (see figure 3.13 b - e ). As seen in the left column of figure 3.13, linear regression was performed for each beam energy to obtain the slope of the respective characteristic line. The intercept of these lines ranges from a 12Bit value of -2,4 to 1,6 and is therefore negligible, i.e. the characteristic lines are described by a purely linear function. As displayed in the right column, an inverse polynomial function of second order was fitted to the slopes of the characteristic lines. The resulting function is used to convert a measurement signal to fluence. Comparing the graphs of

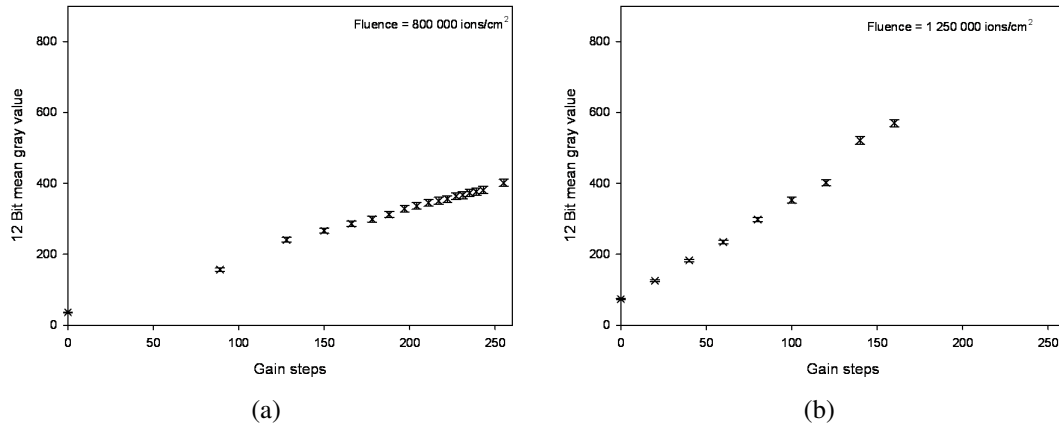


Figure 3.9.: Signal dependence on gain step for two measurements on different days.

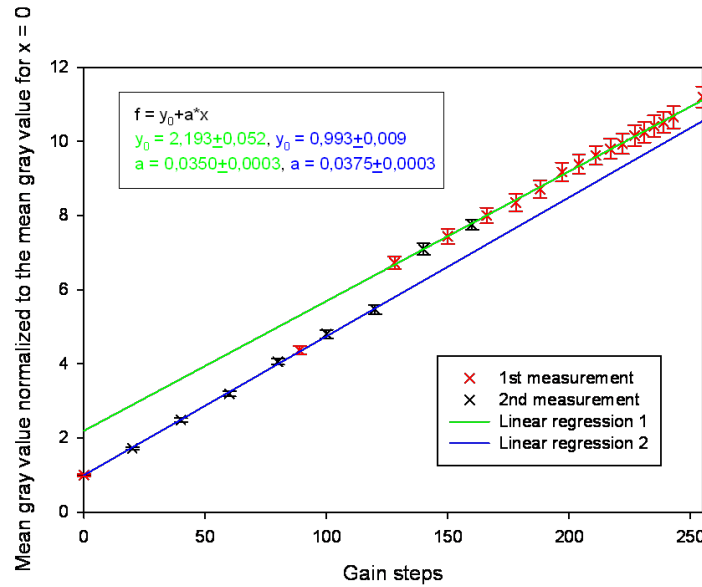


Figure 3.10.: Signal dependence on gain step for two measurements normalized to the gain 0 signal.

figure 3.13b and c, a difference of  $(18 \pm 1)\%$  (referring to the first measurement shown in figure 3.13b ) can be observed over the whole energy range.

### 3.2.3. Application to Patient Treatment Plans

Figure 3.14 shows exemplarily a comparison between planned and measured fluence distributions for two iso-energy-slices of a carbon ion treatment field. Due to the day-to-day variation of the Fluence-calibration curves (see section 3.2.2.2 ) and since it was not possible to repeat the measurement including a calibration on the same day, only the relative rather than absolute fluence distributions were compared. For this, the distributions were normalized to their maximum value. Comparing the planned and measured fluence distributions qualitatively (3.14a to 3.14b and 3.14c to 3.14d ) results in good agreement, as the most prominent features of the

### 3. Results

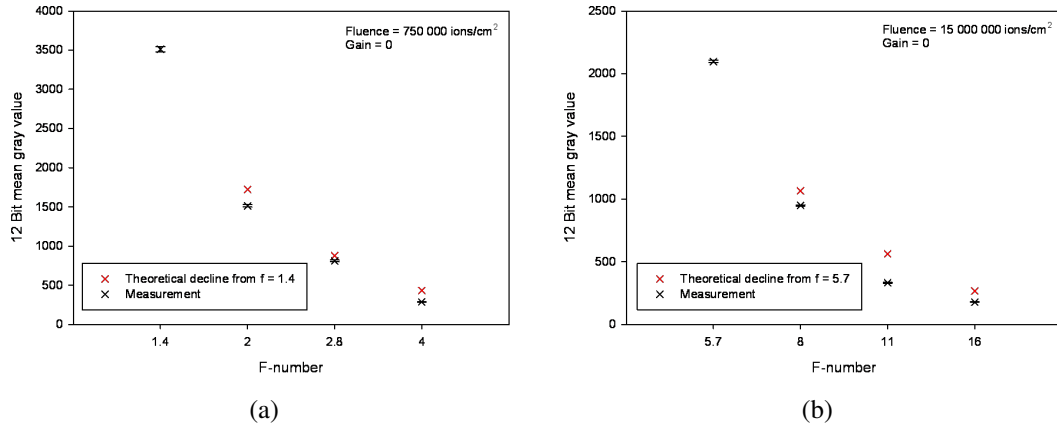


Figure 3.11.: Signal dependence on lens aperture measured for two different fluences.

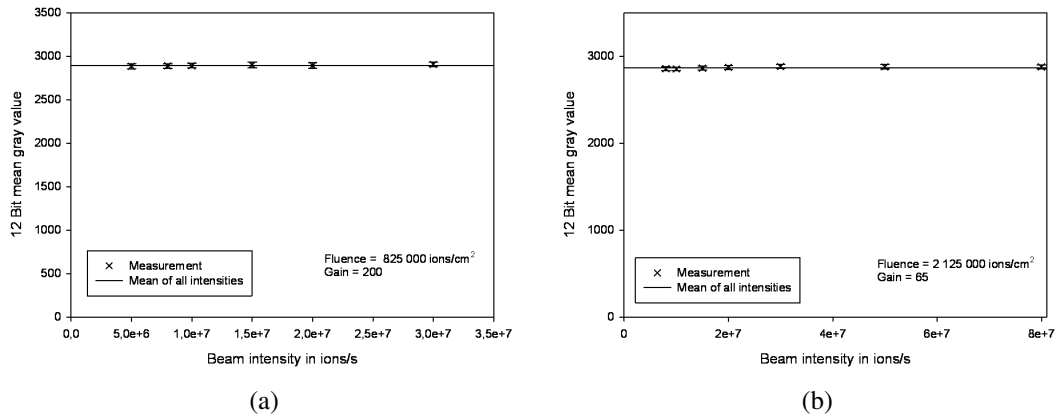


Figure 3.12.: Signal dependence on beam intensity for two different fluences.

planned energy slice can all also be found in the measurement. The dark spots at the center of 3.14b and 3.14d indicate the donut effect.

Nevertheless, the difference maps (3.14e and 3.14f) show large deviations of up to 15% for a relatively homogeneous distribution (e) and up to 30% for a distribution with small hot spots (f). On closer investigation of these maps, one finds a ring, where the agreement is relatively good and two adjacent rings on both sides where the measured values are larger than the calculated ones, which might be explained by a broader signal distribution in the measured image (see discussion). This is supported by an investigation of the horizontal profiles through these distributions (3.14g and 3.14h), which indicate that the measurement is broader by approximately 0.8mm (g) and 1.6mm (h). The focus sizes used in these distributions were 10.1mm (g) and 10mm (h) at the full width half maximum. As an additional test, in images 3.14b and 3.14d, where two hotspots occur, the maximum value of the upper left hotspot was compared with the one on the lower right side of the distribution. This test resulted in a ratio 1.22 between both peaks in the planned distribution and a ratio 1.12 in the measured distribution, respectively,

which indicates that the relative distribution is not exactly the same either.

### 3.2.4. Depth-dependent Response

Figure 3.15 shows measurements of a single beam spot using four different beam energies corresponding to water-equivalent ranges between 3.7 and 27.5 cm. The signal was integrated over the whole beam spot and the curves were normalized at 3.7cm depth. Comparing the results obtained with the scintillating screen detector with the Bragg-Curves used for treatment planning at HIT, which serve as gold-standard here, one finds an increased quenching with depth. At the Bragg-peak position a signal deviation of up to 100% was obtained. Nevertheless, the distal edge of the Bragg-peak complies within 1mm for all energies except for 300MeV/u showing a difference of 2.3 mm.

### 3. Results

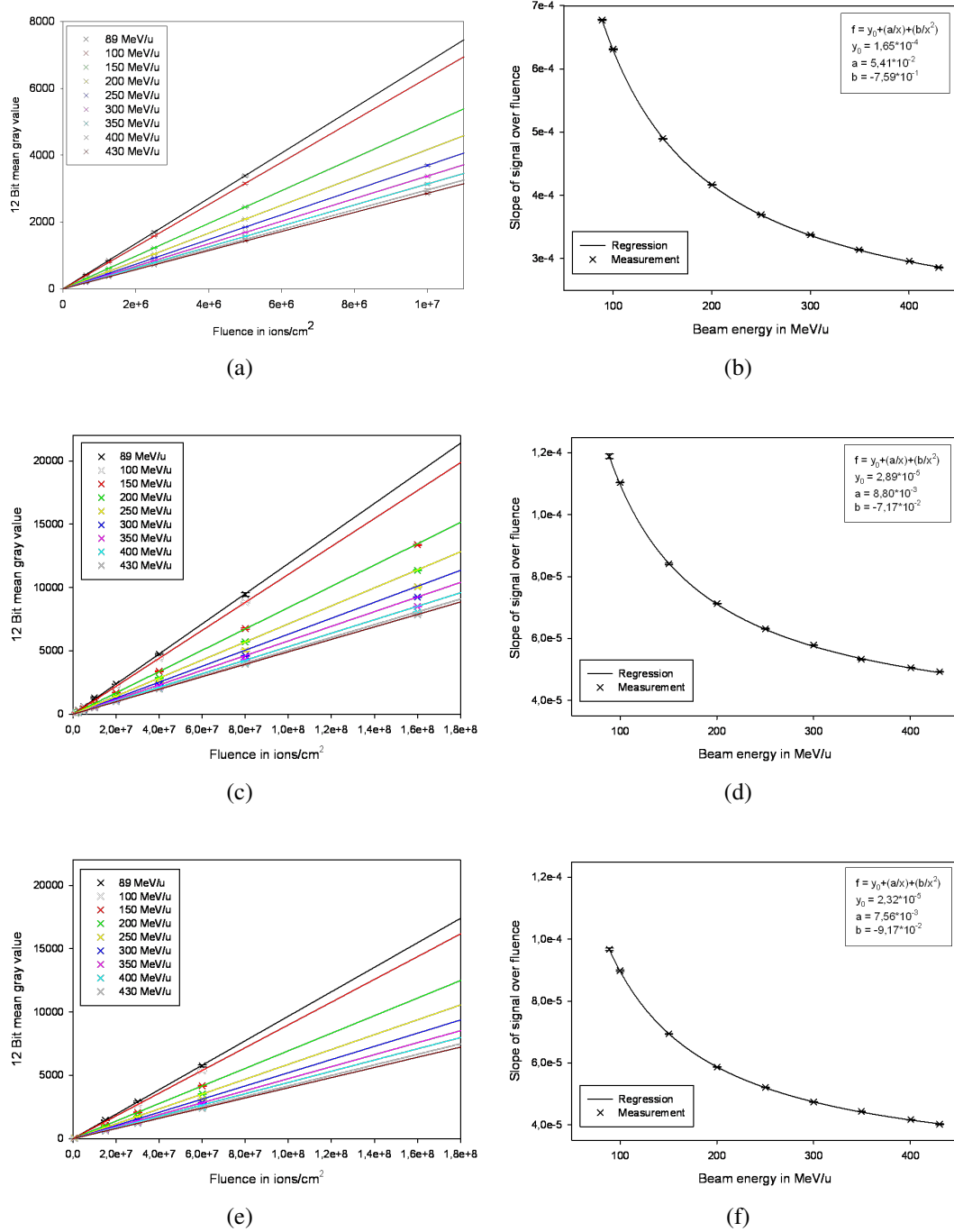


Figure 3.13.: Characteristic lines showing the signal dependence on fluence for 9 beam energies (left) and regression function of the respective slopes (right, gain 0). (a) and (b) F-number 4. (c) and (d) F-number 8. (e) and (f) Additional fluences measured for f-number 8 on a different day.

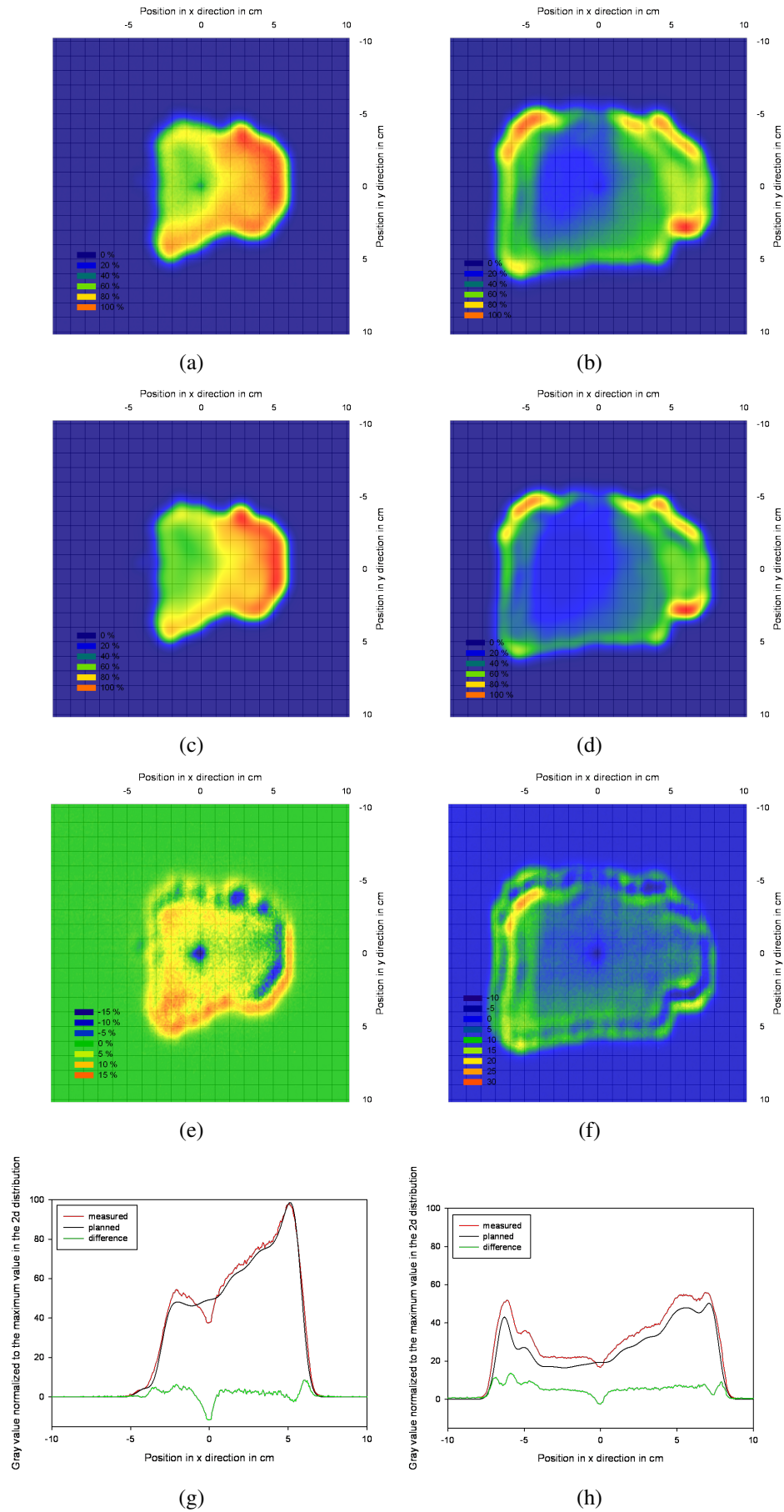


Figure 3.14.: Comparison between measured (a, b) and planned (c, d) carbon ion fluence distributions for two iso-energy-slices of a carbon ion treatment field. Each distribution is normalized to its maximum value. In the difference-maps (e, f) and in the horizontal profiles through the isocenter (g, h) a positive difference value indicates a higher measurement value.

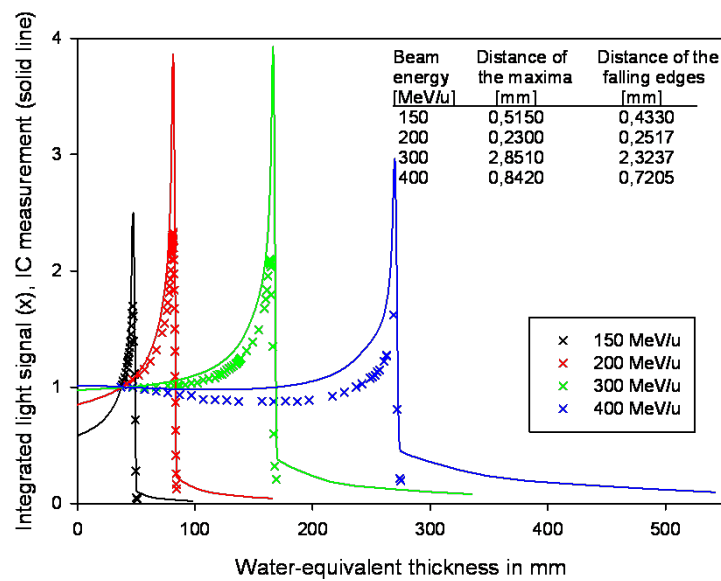


Figure 3.15.: Comparison between the depth dependence of the integrated scintillating screen signal of a single beam spot and the depth profiles used for treatment planning at HIT. The measurements were obtained with constant fluence and normalized to the signal at the minimum water-equivalent thickness of the water column.



## 4. Discussion

Scanned heavy ion radiotherapy as well as Intensity Modulated Radiation Therapy (IMRT) allows highly conformal irradiation while sparing the surrounding normal tissue. As both delivery techniques are very complex, correct beam delivery with respect to geometry and dose has to be assured by measurements of individual patient plans as well as regular quality assurance measurements. As scintillation screens offer high resolution 2d measurements with an optical signal showing linear response to the absorbed dose, they have been investigated for quality assurance measurements in both irradiation techniques.

Here, studies on scintillating screen usage in IMRT and ion beam radiotherapy are presented followed by a discussion of the results obtained in this work. In both parts special emphasis is put on the corrections on the obtained images required by the optical system consisting of the scintillation screen, a CCD camera and, depending on the specific setup, a mirror.

### *Scintillating Screens in IMRT*

At the Stanford University School of Medicine, Stanford, California, two scintillator screen systems were developed, one for fluence and one for dose measurement [44, 45]. For their fluence measurement system (fig. 4.1), called Wellhöfer Beam Imaging Device (BIS), a  $Gd_2O_2S$  scintillation screen with a Cu layer, serving as signal enhancer, is positioned perpendicular to the beam and a CCD camera captures the light signal viewed through a  $45^\circ$  mylar mirror. It is fastened to the blocking tray holder of the linear accelerator and rotates with the gantry. The images are calibrated pixel by pixel by first subtracting the background signal and then dividing by a calibration factor obtained from uniform x-ray beam geometry. Then, a correlation method is used to compare the measured images with reference images calculated from dynamic Multi leaf Collimator (MLC) leaf sequencing files. The investigated IMRT fields resulted in a correlation coefficient of  $> 95\%$ , which can be compared to a value of  $-10\%$  to  $-15\%$  resulting when the measured fields are correlated to the mirror reflection of the respective reference files. This indicates that this procedure can be used to online detect simple errors in leaf sequencing files.

Their design for dose measurement is called Wellhöfer Water Beam Imaging System (WBIS) and consists of a plastic scintillator screen inserted into the center of a Plexiglas cylinder with 20 cm of water on either side of the screen. A CCD camera is placed opposite to the screen and the detector is placed with the screen in the isocenter and perpendicular to the gantry (fig.

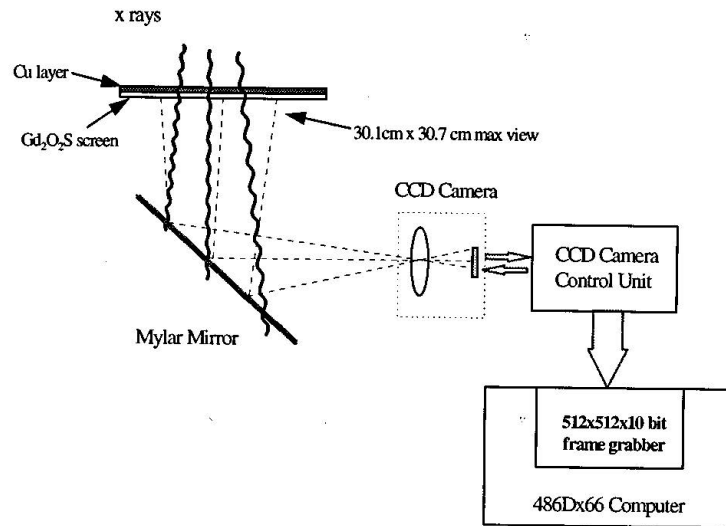


Figure 4.1.: Detector setup as illustrated in [44].

4.2). For dose verification, 200 images are acquired per field, background-corrected and only an inner circle with a diameter of 25 cm is taken into account. Scattering in the scintillator, the water and the glass window in front of the camera results in a blurred image, which needs to be de-convoluted with a point spread function (PSF) consisting of a double Gaussian. The PSF is determined comparing a measured image and a Monte Carlo (MC) simulation and then used in an iterative procedure to find the de-blurred image. Then the image is calibrated by first performing a flood-field correction, for which the detector is irradiated with a uniform x-ray field to find a correction for intrinsic response inhomogeneities. The correction factor is obtained by comparison of the image of the uniform field with the respective MC simulation. During calibration each pixel value is also corrected for its distance to the CCD camera. Finally, the results are compared with dose distributions from the planning system or from MC. With this system an agreement of 3% of the maximum dose was achieved comparing a measured and MC simulated open field, excluding the field edges, and of 5% comparing both results of a clinical case.

Petric et al. developed a plastic scintillator based, water-filled dosimetry system with a different design [46]. Here, the scintillating screen is placed perpendicular to the beam and on top of a water-filled Lucite phantom that contains a silver coated plastic mirror at a 45° angle towards the beam. The scintillation signal is then reflected by the mirror through a clear viewing window towards a CCD camera. Additional blocks of tissue equivalent material can be added on top of the scintillator (fig. 4.3). In this system, the main source of optical scattering and hence blur is multiple reflections between the screen and the mirror. This spatially variant scatter is corrected for by introducing a microlouvre light control film directly below the film, as earlier described by Partridge et al. [47]. Additionally, spatially invariant scatter occurs in the water and Lucite

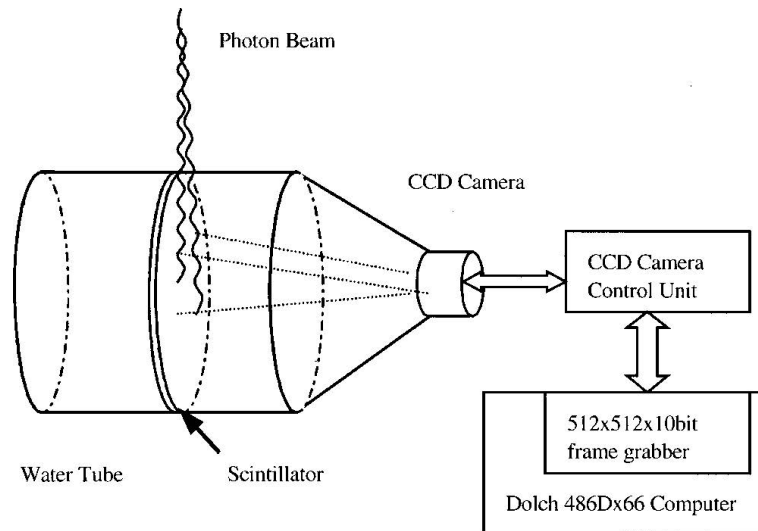


Figure 4.2.: Detector setup as illustrated in [45].

window. This is again removed by de-convolution with a blurring kernel. Due to the previous filtering step, the PSF is fitted with elliptical Gaussians, for which the empirically established relation between pixel address and object plane point is also considered. The PSF is optimized using Wiener filter fast Fourier transform (FFT) and the same technique is used to de-convolve the PSF from each image. Additionally, again a flood-field correction is performed. Finally, the light distribution map is converted into a dose distribution map with a factor from linear regression of measured dose-response-curves. For this system, a signal uniformity of 5.6% and long-term stability of 1.7% were found. For measurement of 2d distributions, agreement within 8% compared to film measurements was achieved.

A detector called DOSIMAP was developed by Collomb-Patton et al., in which a plastic scintillator is placed perpendicular to the beam on a transparent polystyrene cubic that contains a mirror in a 45° angle towards the beam [48]. The signal reflected by the mirror is again recorded by a CCD camera and additional polystyrene can be added on top of the scintillator (fig. 4.4). The parasitic Cerenkov light that is produced in the polystyrene is separated from the scintillation light by modulating the scintillation light via a mask placed between the scintillator and the polystyrene block. Due to simple periodic modulation, the signal is concentrated in only one location of the Fourier plane, so that the Cerenkov signal can be suppressed during demodulation. Additionally, hotspots are filtered out of the images and again a flood-field correction is performed against film measurement. Finally, the signal is absolutely calibrated against an IC measurement. With this system, an agreement with IC measurements within  $\pm 2\%$  is achieved for photon depth-dose curves and within  $\pm 4\%$  for electrons. The repeatability is better than  $\pm 2\%$  for small doses and better than  $\pm 1\%$  for doses higher than 0.5Gy. When DOSIMAP is compared to film for IMRT fields, it fulfills a gamma-index of 3% and 3mm everywhere.

Wiezorek et al. compared the MapCheck diode system (Sun Nuclear), the IMRT QA scin-

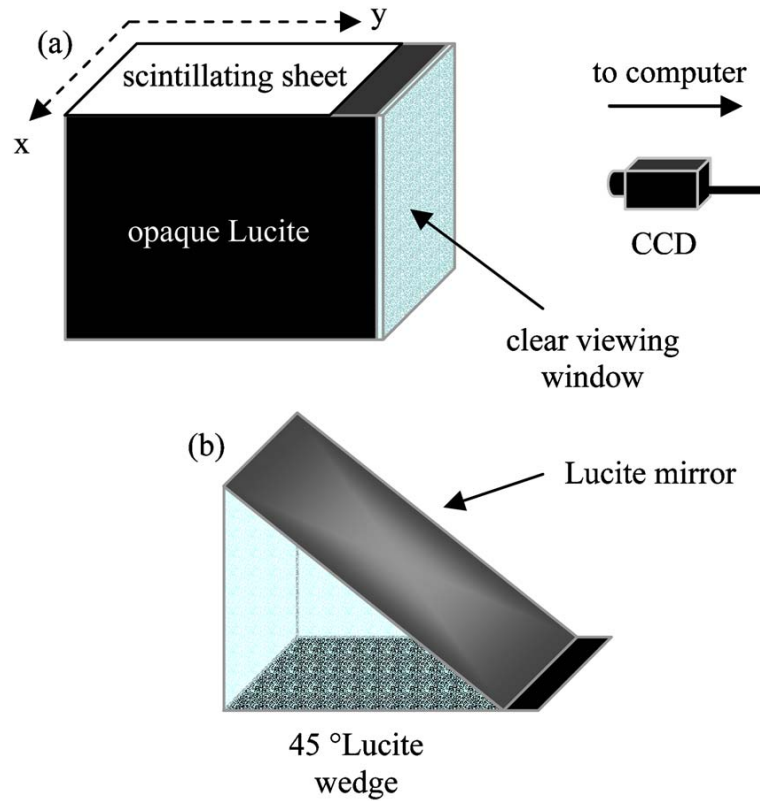


Figure 4.3.: Detector setup as illustrated in [46].

tillation detector (Scanditronix/Wellhöffer) and the Seven29 IC array (PTW) in order to find a 2d detector that can replace film measurements in IMRT [49]. The I'mRT QA detector consists of a brass alloy coated with  $Gd_2O_2S$  placed perpendicular to the beam and the scintillation light reaches the CCD camera via a mylar mirror positioned at  $45^\circ$  towards the beam [50]. The results obtained with these detectors were compared to treatment-planning calculations, film and various point dose detectors. In relative dose measurements of IMRT fields, they found an agreement of better than  $\pm 5\%$  for all detectors and state that the scintillation detector offers a better resolution and larger field size than the others, but can be used for relative dosimetry only.

### *Scintillating Screens in Ion Therapy*

Boon et al. developed and tested a scintillating screen detector to be used with scanned proton beams [51,52]. The detector consists of a  $Gd_2O_2S:Tb$  screen with tissue equivalent material on top placed perpendicular to the beam and a mirror at a  $45^\circ$  angle reflects the light distribution to a CCD camera placed behind lead shielding at  $90^\circ$  towards the incoming beam (fig. 4.5). This setup differs from those presented in the previous section by a larger distance between mirror and screen and by absence of a metal plate at the back of the screen. The mirror distance was chosen to prevent image distortions from light backscattering from mirror to screen and a metal plate is not necessary. The system also has a large distance between screen and camera, which

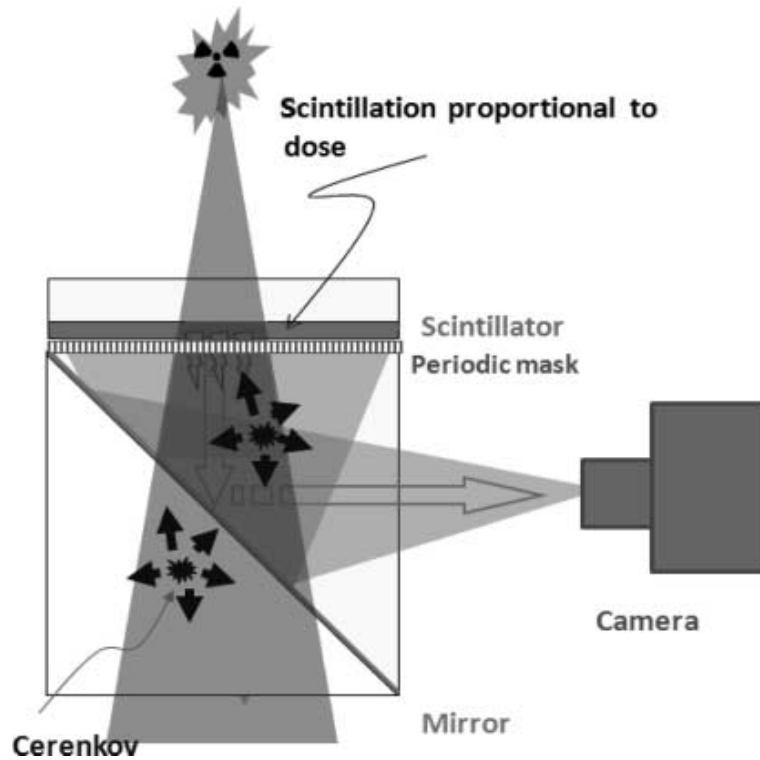


Figure 4.4.: Detector setup as illustrated in [48].

reduces the vignetting effect to 0.4% and is therefore neglected.

This system was extensively investigated and image correction methods established. Several sources of noise were identified for this setup. Random noise can be caused by a statistical variation in the energy deposition process as well as by the measurement itself. Here, the signal-to-noise ratio of 102 was found. Additionally, background is caused by the dark current of the camera depending on the temperature, which can be neglected for the camera in this setup, and by ambient light, which can be removed from the signal by subtracting a dark image with the same integration time. Another contribution results from x-rays,  $\gamma$ 's or neutrons directly interacting with the CCD chip. This contribution is proportional to the delivered dose and in this case corrected by subtracting two images and building the absolute result pixel by pixel. If these values exceed a threshold, the peak is assumed to be noise and the minimum of the corresponding source images is used. If the threshold is not exceeded, the source pixel values are averaged. Further, a spatial resolution of 1.3mm was found with negligible blurring and a comparison between calculated and measured yield showed an agreement within 5%. An investigation of quenching resulted in a deviation of up to 8%.

As presented by Schippers et al., the aforementioned system can be used to measure the alignment of beams used for therapy (photons as well as ions) and to perform an alignment verification of the total treatment system [53, 54]. For that purpose, a sphere is fixed to the patient positioning table and positioned at the isocenter and the scintillation detector is attached to the

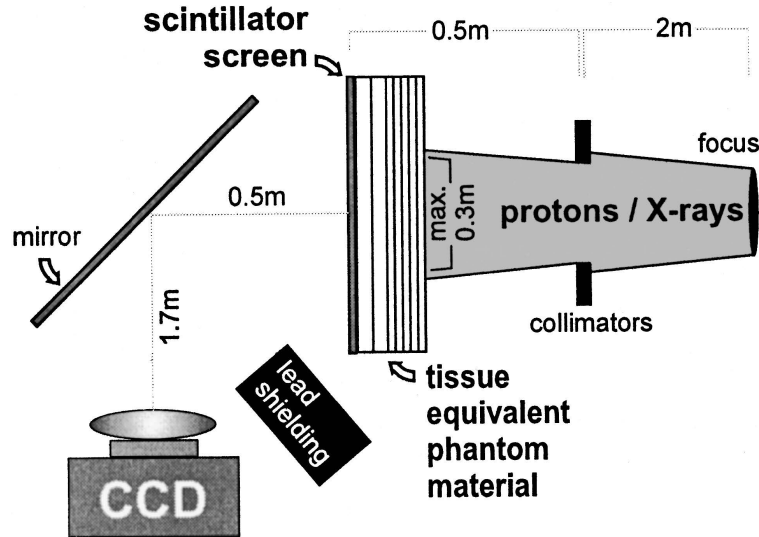


Figure 4.5.: Detector setup as illustrated in [51].

gantry downstream of the sphere. When the detector is irradiated by a circular beam, the sphere generates a shadow in the detected image and the shadow position with respect to the measured spot allows the detection of misalignment with an accuracy of 0,05 mm.

The system was also investigated for 2d dosimetry at the scanning proton beam facility at the Paul Scherrer Institute [54, 55]. A whole field was recorded in one CCD measurement with noise of about 0.5% in each pixel. For these measurements, the conversion factor from signal to dose was obtained with a Markus IC as gold-standard. The measurements resulted in no dose-rate-dependence. An investigation of measurements of small beams, as used for example in eye treatment, showed that blurring can be ignored for fields with a diameter larger than 4mm, but reduces the dose maximum by 5% for a 2 mm beam. The detection of inhomogeneities in a 2d dose distribution resulted in an estimated detection limit of an artifact of 0.5% of the dose. Further, a semi-3d verification was performed by irradiation of a 3d box-shaped dose with a missing spot causing severe underdosage with the detector placed at 6mm depth. This severe underdosage could easily be detected and it was concluded that the sensitivity of the system is sufficient to detect important deviations of approximately 10%, but not to detect deviations in pencil beams with a lower weight.

At the HIMAC experimental port a scintillation detector system was tested with carbon ions developed by Furukawa et al. [56]. This setup aims to reconstruct the 3d dose distribution in the target volume from slice by slice fluorescence measurements of a scanned beam. It consists of two parallel-plate ICs (main monitor) placed just downstream of the vacuum duct, a fluorescent screen made of  $Gd_2O_2S : Tb^{3+}$  on polyethylene terephthalate positioned downstream of the range shifter at a  $45^\circ$  angle but upstream of the isocenter and a cooled CCD camera looking at  $45^\circ$  on the screen (fig. 4.6). The whole system is surrounded by a dark box and attached

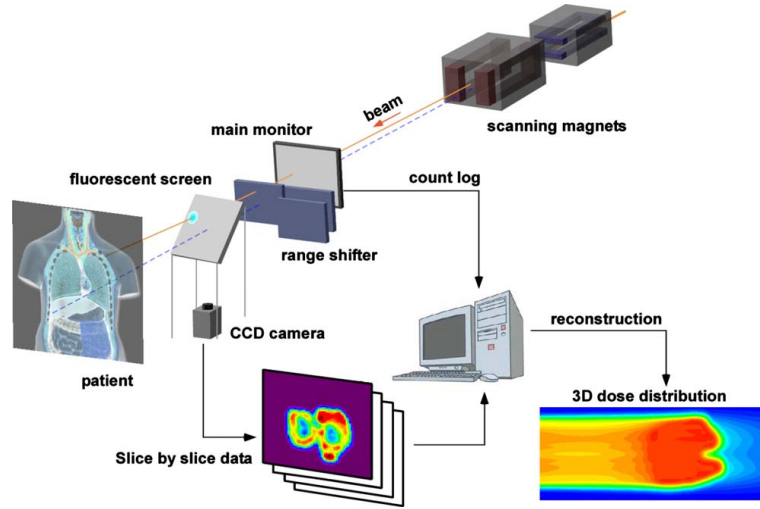


Figure 4.6.: Detector setup as illustrated in [56].

to the beam nozzle and during the measurement procedure the camera integrates over each energy slice. The images are then processed offline by first subtracting background according to the respective measurement time and then applying a median filter to remove spike-like noise. The next step is a perspective transformation, as the camera is not mounted perpendicular to the screen; it also includes a bi-linear interpolation to convert the pixel size to  $1\text{mm}^2$ . At last, a flood-field correction is performed and the 2d fluence distribution at the screen position is obtained by summing up all 2d distributions of the field. Alternatively, to obtain the 3d dose distribution each slice is further processed by iteratively de-convolving it with a Gaussian kernel resulting in a 2d weight map, which contains the particles numbers per spot. The irradiation steering file is used as initial condition of the weight map. Subsequently, the integrated weight map is normalized to the count obtained with the main monitor and thereby quenching can be excluded from the calculation. Then a 3d weight map is obtained and superimposed with the dose kernel of a premeasured spot beam to calculate a 3d dose distribution. This system was then tested for patient irradiation plans and the results were compared to those made with a cross shaped  $64 \times 64$  IC array. This comparison resulted in a maximum deviation of 5% in the target volume.

#### 4.1. Image Scale and Corrections

This section discusses the measured and calculated image corrections, as well as their uncertainty and application to measured images.

#### 4.1.1. Pixel Scale

A small but significant difference was found in the pixel scale between Detector-E and Detector-H. As the same camera and lens combination is used in both detectors, a slightly different lens-screen-distance is assumed to be the source of this deviation. As the camera could not be detached, however, this could not be finally confirmed. As a consequence, two different pixel scales were used with both detectors.

#### 4.1.2. Background Correction

Before the mean background signal without irradiation was subtracted, a median filter (radius = 2) was applied, reducing random noise to a minimum and, therefore, resulting in a background signal that consists solely of an offset value (figure 3.1a). The same procedure was performed for subtracting the background of irradiated images, which show peaks caused by neutron interaction with the CCD-chip of the camera additionally to the white noise of non-irradiated images. However, as the median filter reduces these peaks to a minimum as well, the background in irradiated images can also be approximated as an offset value after filtering.

When this offset value was measured for gain values between 0 and 255, a gain dependence was observed. When testing the gain dependent offset values on their stability over time, significant deviations were found for measurements on two different days (figure 3.2a). Although the offset values on both days still follow the same gain dependent pattern, the ratio between gain 0 and gain  $x$  is different in both measurements.

This suggests that it is not possible to perform a series of gain dependent offset measurements that can then be applied to all following scintillating screen detector measurements. Instead, the actual offset value has to be recorded before each measurement session and can then directly be applied to the measured images. As the offset is gain dependent, a separate offset measurement needs to be performed for all gain values that are used in that session. However, for the measurements presented in this work, the offset value was subtracted from the images offline after the images were recorded, not during measurement and storage.

An investigation of the homogeneity of the filtered background distribution for the image area, which is corresponding to the field of view of the accelerator, showed that even for the highest gain value the residual noise in the offset value is small and homogeneously distributed (figure 3.2b). Therefore, this whole area outside the irradiated field can be averaged to find the best offset value for each measurement session and gain setting.

Further, as the mean background was neither increased by prolonged exposure times nor by usage of a larger aperture (figure 3.2c and d), it can be concluded that light from sources outside the detector does not contribute to the background signal.



### 4.1.3. Lens Corrections

#### 4.1.3.1. Geometrical Distortion

As the investigation of millimeter paper resulted in a negligible geometrical error, no distortion correction was introduced into image processing.

#### 4.1.3.2. Vignetting

##### *Establishment of a homogeneous Light Source*

Scanning the lightfoil in  $2 \times 2 \text{ cm}^2$ -pixels, a correction could be found reducing the systematic light-density decrease over the area of the lightfoil to 0 and leaving random deviations below 3% (referring to the central value) minimum to maximum (figure 3.3), which is a very low value and can be compared to a homogeneity of  $\pm 4\%$  of a Ulbricht sphere, which is a frequently used instrument to measure artificial vignetting of camera lenses. However, one has to keep in mind that the 3% refer to mean values of  $2 \times 2 \text{ cm}^2$ -pixel and individual deviations on a smaller scale might be higher and may require filtering of the vignetting measurement performed with the lightfoil.

##### *Determination of the Vignetting Correction*

The images that were taken to determine a vignetting correction show the expected darkening towards the outer parts of the image. The profiles for small f-numbers, presented in figure 3.5, therefore show symmetric behavior and a vignetting effect that is stronger for decreasing f-numbers. For f-numbers 4 and higher, however, this symmetric behavior is superimposed with an asymmetric effect that is more pronounced for increasing f-numbers and dominates the profile for f-numbers 11 and 16. The same effect can be seen in the 2d distributions in figure 3.4. This behavior was found in two independent measurements. External light sources that might have been present during the measurement could be ruled out as the source of this asymmetric behavior, as the measurement was performed for several distances between the camera and the lightfoil and the same effect was observed although different sections of the lightfoil were recorded. The measurement was also performed with different orientations of the lightfoil, so that a residual systematic drift in the light distribution can be ruled out as well, as the asymmetry always occurred in the same direction independent from the orientation of the lightfoil. Therefore, it is assumed that asymmetry is caused by the lens itself. This specific lens is designed with only 5 blades and contains a dark plate in the center of the lens, which is used to achieve very large f-numbers with this lens in other applications, such as room surveillance. When the blades are closing, they cannot form a perfect circle around the dark plate in the center of the lens. This may prevent light from entering the lens which may result in the observed asymmetric effect for the vignetting function.

Although a vignetting effect with asymmetric characteristics can be corrected as described in

the following section, using a different lens that does not show asymmetric behavior might result in a higher accuracy. Using the current lens with f-numbers  $< 4$  only might improve the accuracy as well. In this work images of the lightfoil were taken for all available f-numbers and corrected for the lightfoil's in-homogeneity. As a result, a two dimensional vignetting function was obtained for each f-number. To eliminate the short-scaled intensity-variations of the light foil, which could not be compensated by the above in-homogeneity correction, a median filter with a radius of 100 was used on the average of two two-dimensional vignetting images obtained with the same aperture. The resulting two-dimensional functions are used for a pixel by pixel vignetting correction for all measured images, according to the aperture used during measurement.

#### **4.1.4. Effects of the tilted Screen**

Both, the geometric and intensity correction for the tilted screen were tested successfully with raster (figures 3.6 and 3.7) and homogenous fields (figure 3.8). The dominant part of the geometric correction is a factor representing the image elongation in horizontal direction due to the  $45^\circ$  angle. The additional replacement only results in shifts of up to  $1.5\text{mm}$  on a  $10\text{cm}$  scale, while the intensity correction accounts for about 3% on the same scale. In both cases the correction is minimal in a center region of  $5 \times 5 \text{ cm}^2$ . The calculated correction functions are used in the processing of each image before further evaluation.

## **4.2. Investigation of Detector Response**

In this section, initial irradiation measurements are briefly discussed, before the fluence calibration and its application to patient plans is described in more detail. Finally, it also includes a discussion of the investigation of depth dependence of the detector signal.

### **4.2.1. Signal Dependence on Camera Parameters**

#### **4.2.1.1. Gain**

Measurements of the signal dependence on gain (figure 3.9 and 3.10) resulted in two different linear functions depending on the range of the gain setting. In both cases, similar slopes but different intercepts were obtained. This was confirmed by a second independent measurement with different fluences. It is concluded that gain factors above gain step 0 do not change over time, so that it is possible to calculate the signal for a given gain step, when the signal for gain step 0 is known.

For gain step 0 on the other hand, it was found that the result of both measurements exhibits different signals when normalized to the same fluence. Here a difference of 31% was found, which

is of similar size of the day-by-day variations of the fluence calibration measurements (figure 3.13 b and c), where the signal difference was 18%. The implications of this are discussed in 4.2.2.2.

#### **4.2.1.2. Aperture**

Comparing theoretical and measured signal decrease with increasing f-number, albeit a faster decrease of the measured values, the expected  $1/f^2$  dependence in first order was found with a difference of up to 41% was found.

### **4.2.2. Signal Dependence on Beam Parameters**

#### **4.2.2.1. Beam Intensity**

As no signal quenching was observed with increasing beam intensity, all particle flux settings available for carbon ions at HIT can be used with the scintillating screen detector.

#### **4.2.2.2. Particle Fluence**

Looking at the fluence calibration (figure 3.13), performed with gain step 0, it can be seen that the linear regression lines fit the measured mean signal values with only very small deviations and the same is the case for the inverse polynomial function fitting the obtained slope values for the different beam energies. However, the two measurements performed for aperture f-number 8 (figure 3.13 b and c) lead to significantly different slopes of the characteristic lines and consequentially also to different fitting functions for the slopes. As discussed in 4.2.1.1, similar large deviations were found in the measurement result for gain step 0. Therefore it is assumed that the sensitivity of the camera differs from measurement to measurement although the camera settings are the same. A potential explanation would be a camera-internal electronic adjustment of the sensitivity. This makes it impossible to perform a single fluence calibration that is valid further on for all measurements. As a consequence of this finding, a calibration measurement has to be performed at the beginning of each measurement session. On the other hand, since the characteristic lines show a strictly linear behavior, it is sufficient to measure the signal for one or two fluences for a representative number of energies, which may be performed in less than 5 min. By fitting the slopes as a function of beam energy, the slopes and hence the characteristic lines at other energies can be accurately interpolated.

### **4.2.3. Application to Patient Treatment Plans**

The comparison between normalized planned and measured 2d fluence distributions in two example cases showed severe differences, which are too high for usage of the detector for fluence measurements in quality assurance. However, a characteristic pattern of those differences was

observed in both cases. An outer ring was found where a zone of good agreement or low measured fluence was sandwiched between two zones, where the measured fluence exceeded the expectations. This behavior might be explained by blurring in the measured image, which would cancel out in homogenous regions but would lead to a broadening of the field edges and thereby reduce the maximum dose in that region also. The different ratio between local maximum values found between measurement and calculation supports that hypotheses, as differently shaped maximum regions would be affected differently by blurring also.

To find further evidence, the edges of a  $5 \times 5 \text{ cm}^2$  homogenous field measured with the scintillating screen detector and radiographic film were investigated. Figure 4.7 shows the obtained profiles with reference lines indicating the maximum value, half the maximum value and their respective positions on the left edge of the field. This investigation resulted in a distance between the maximum and half the maximum value of 0.5 cm for the film measurement and of 0.7 cm for the scintillating screen measurement. As the film was positioned 52.1 cm in front of the isocenter due to restrictions in the measurement setup, this width has to be scaled to the isocenter taking a distance to the beam source (here the steering magnet in x-direction) of 649.14 cm into account. This results in a width of 0.54 cm in the film measurement. The decreased slope at the edge of the field for the scintillating screen measurement supports the hypotheses that part of the differences between measured and calculated 2d distributions can be explained by blurring.

As the depth of the scintillator is less than  $100 \mu\text{m}$  [27] and no additional material is positioned between camera and screen, the optical system might be the cause for this effect. This needs to be further investigated and a suitable de-blurring procedure developed.

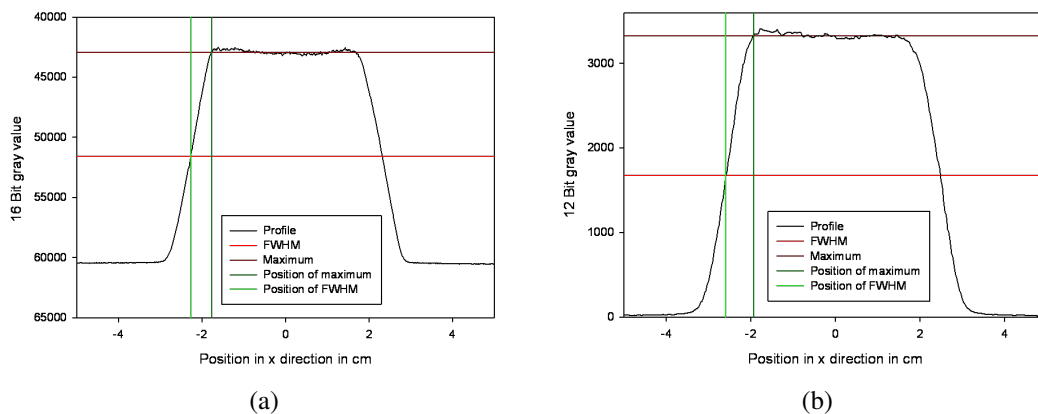


Figure 4.7.: Horizontal profiles of a  $5 \times 5 \text{ cm}^2$  homogenous field measured with (a) radiographic film and (b) a scintillating screen detector.

#### 4.2.4. Depth-dependent Response

To further characterize the scintillating screen detector, the signal dependence on water-equivalent depth was investigated. It was, however, not aim of this work to use the detector for actual dose measurements. First, the results are discussed and then, complementarily, considerations on the usability of a scintillating screen detector for dose measurement are added.

Comparing the 4 resulting Bragg-curves with the gold-standard (figure 3.15), it can be seen that the position of the Bragg-peak can be measured with the water-column-detector setup with an accuracy of better than 0,8mm, except for the measurement of an initial beam energy of 300MeV/u, which shows a larger deviation of more than 2 mm. This is assumed to be caused by positioning the water column not exactly perpendicular to the beam, thereby increasing the range in water. However, these measurements serve only as a consistency check, as the setup is time consuming and error prone, whereas better detectors exist for range measurements, such as the PEAKFINDER (PTW, Freiburg, Germany) [18]. The measurement shows that a quenching correction is already necessary at water depths of a few centimeters.

Generally, dose calibration is not a straight forward procedure for any detector that shows quenching, as quenching disturbs the unique relation between signal and dose. The ratio of signal to dose depends on the LET, correlating with the residual energy or depth in water, respectively. It also depends on the initial beam energy, as two beams of carbon ions, which started off from different initial energies, but have reached the same residual energy, did undergo a different fragmentation process and, therefore, exhibit a different LET spectrum.

In raster scanning, a mono-energetic, two-dimensional irradiation field is applied slice by slice and the verification procedure is performed slice by slice as well. As for a constant initial beam energy and measurement depth the ratio of signal to dose is constant as well, dose calibration can be performed for this beam application and measurement method. For that purpose depth-dose-distributions need to be recorded for all available initial beam energies and correlated to ionization chamber measurements or Monte Carlo calculations serving as gold-standard. The number of measurements may be reduced by developing a model for the LET-dependence, which allows parameterizing the signal dependence in a way that for example the dependence on LET can be replaced by a dependence on residual path length. Measurements may also be partly replaced by Monte Carlo techniques [57], where the quenching model has to be included. In that context, Beddar et al. [58] showed for proton irradiation that the signal response of a liquid scintillator for low energies can accurately be modeled with GEANT 4.9.1 Monte Carlo including the two-parameter Birks function.

However, dose-calibration would be much easier, if quenching was avoided. Safai et al. [59] investigated this possibility for proton irradiation. They found that (Zn, Cd)S:Ag shows increased scintillation efficiency for an increasing LET. Mixing this material with a scintillating material with decreasing scintillation efficiency allowed modulation of the height of the Bragg peak and reproduction of ionization chamber measurements without quenching. It might be promising to

investigate this approach for carbon ions as well.

Here the integrated depth profiles were measured. The current detector geometry does not allow measurements of dose or fluence distributions in depth, because it is not possible to place water-equivalent material parallel to and directly in front of the scintillating screen. This poses a problem, as an air gap between material and screen changes the fluence distribution. This effect is enhanced for an increasing distance. This effect is very difficult to correct, especially for a non-constant distance between material and screen. In our initial measurements, this was considered by integrating over the whole irradiation field.

### **4.3. Usage of the Scintillating Screen Detector**

Subject of this work was an investigation of a preexisting detector system that is currently used for tuning of the beam alignment. The aim was to assess its usability for fluence measurements of 2d distributions in patient plan verifications and general quality assurance and to develop necessary adaptations. While further investigation, beyond the scope of this work, is necessary to use the detector with a sufficient accuracy in quality assurance measurements, a procedure to obtain fluence maps was developed incorporating image corrections and calibration of the system. Here, this procedure is described and additionally system characteristics are discussed that should be considered, when a scintillating screen detector system to be redesigned.

#### **4.3.1. Fluence Measurements with the current System**

To obtain fluence maps with the current scintillating screen detector system, first the entrance of the detector is covered with black foil. It also has several open junctions around the detector that have to be covered as well. Additionally, the brightest light sources, like monitors for example, should be covered and later during measurement the light should be switched off.

Next, the detector has to be positioned in the treatment room with the center of the screen aligned with the beam isocenter (compare image 211). In the horizontal treatment rooms the detector is moved with a robotic arm and at the experimental beam line it is placed on a table adjustable in height and positioned by hand to match the room lasers.

After that, the detector is connected with the camera control unit, which has to stay switched off during connection, and the control unit is connected via firewire with the measurement laptop, which runs the camera control and measurement software and will stay in the treatment room during measurement. For that reason a network connection is established between this laptop and another computer outside the treatment room. The aperture control (compare image 2.9) unit is also attached to the detector and the desired aperture is chosen. Then, the trigger entrance of the control unit is connected to a system providing the beam on signal from the accelerator.

The trigger control modus of the camera shutter is used for all measurements with beam; for the measurements without beam to obtain background images and images of the laser cross, a predefined integration time is used.

After these preparations, a hatch at the rear side of the detector is opened allowing the laser beam to enter the detector so that an image of the laser cross can be taken. After this measurement the hatch is closed again. Alternatively, a cross pattern marking the isocenter can be irradiated and measured. Now, the detector is irradiated with a part of the each irradiation plan scheduled for the respective session, which contains the highest fluences and lowest energies. This irradiation is used to optimize the gain value that will be used for measurement of each plan to about 80% of the measurement range.

At this point, the fluence calibration, which is described in 2.4.2.2, is repeated with two fluences, e.g.  $6.25 * 10^5 \text{ ions/cm}^2$  and  $1.25 * 10^6 \text{ ions/cm}^2$ , for different energies, e.g. 100 MeV/u, 150 MeV/u, 200 MeV/u, 300 MeV/u and 400 MeV/u. This is done for each gain that is being used in the measurement session. The obtained gain value for each irradiation plan is subsequently used to measure two background images. These measurements are directly median filtered (radius = 2) and the mean value of a 20x20 cm<sup>2</sup> field is determined as background, and the average value of both background images will be subtracted from respective measurements before the images are further processed.

After that, all patient plans can be irradiated and recorded spill by spill. Offline after the irradiation, all corrections are applied as described in 2.4 except for the offset correction, which is already considered during measurement. Subsequently, the slopes of the measured characteristic lines are determined and their energy dependence is fitted with an inverse polynomial function of second order. The slope for each energy slice of an irradiated plan can be interpolated with this function and then be used to convert the 2d signal map into a fluence map. The result is stored in a data file and can be displayed and further evaluated.

#### **4.3.2. Considerations for Construction of a Scintillating Screen Detector**

The investigation of image corrections required by the current scintillating screen detector revealed some disadvantages that should be considered if a new detector system is build with the aim of using it for fluence measurements.

First, investigation of the background showed an offset value superimposed with white noise. Here, the white noise is in first order corrected by applying a median filter (radius = 2). Its appearance could, however, be reduced by using a cooled camera. To additionally reduce background peaks for irradiated images, the camera could be shielded to reduce the interaction of neutrons with the CCD chip. Further, the offset value differs from day to day, so with a camera with a time-independent offset the offset measurements before each session could be avoided.

When vignetting corrections were measured, asymmetric behavior was observed. The five-blade iris and a dark plate, which is positioned in the lens center, were suggested as the source

for this asymmetry. Although asymmetric vignetting functions can be corrected for, a higher accuracy and reliability would be expected for a lens that has an iris with more blades and no dark plate.

In gain dependence measurements as well as in fluence calibration measurements a day-by-day difference of the sensitivity at gain step 0 was observed. This finding requires a new fluence calibration in each measurement session for the current detector, which could be avoided with a camera showing time-independent sensitivity.

It was discussed that the current setup for beam, screen and camera is suitable for fluence measurements after corrections are applied. Nevertheless, if the detector was intended to be used for measurement in depth, it would have to be changed. This is required, because the current setup does not allow placing material parallel to and directly in front of the screen, leading to a laterally increasing air gap behind the material, and hence to a position-dependent change in the fluence distribution.

Further, with regard to measurements in depth, quenching was found in initial measurements requiring extensive measurements or elaborate simulations. Safai et al. [59] showed an interesting approach for proton irradiation to avoid quenching by mixing scintillator materials with different quenching behavior.



## 5. Conclusion

In this work a scintillating screen detector system at HIT, which was originally developed for beam diagnostics, was investigated for usability in fluence measurements.

Measurement control and evaluation software was developed and implemented. Further, a method was developed to establish a homogenous light source to be used in the measurement of lens vignetting corrections. In addition, background and perspective corrections for the scintillating screen systems were developed and implemented in the software. The response of the detector system was characterized for different camera settings and beam parameters. The detector showed no dependence on beam intensity and the dependence on fluence was strictly linear with an energy-dependent slope. As the fluence calibration has shown a large day-by-day variation, a recalibration is required for each measurement session.

To measure 2d fluence maps with this system, a procedure was defined that includes determination of the isocenter, gain optimization, background measurements and fluence calibration as a prerequisite of each measurement session. The actual measurement is performed spill by spill using a trigger signal and the result is recorded in .tiff images. With this procedure, the system is characterized and can now be used to measure 2d fluence distributions. Comparisons of measured and calculated 2d fluence maps of treatment plans showed broader distributions in the measurement. This was attributed to an optical blurring effect, which has not been corrected for and which has to be further investigated before the system can be used clinically.

Finally, the system was used to measure depth dose distributions, which resulted in signal quenching showing the LET-dependence of this detector. The measured Bragg-peak position agreed well with the expected position.

The results obtained with the system were used to derive general requirements for the design of an optimized scintillating screen detector.



## References

- [1] S. Nill, R. Hinderer, and U. Oelfke. *X-IMRT*, chapter 23.
- [2] G. Kraft. Tumorthrapy with ion beams. *Nuclear Instruments and Methods in Physics Research. A* 454:1-10, 2000.
- [3] H. Krieger. *Grundlagen der Strahlenphysik und des Strahlenschutzes (3rd ed.)*. Teubner, 2009.
- [4] H. Paganetti and T. Bortfeld. *Proton Therapy*, chapter 27.
- [5] M. Torikoshi, S. Minohara, N. Kanematsu, M. Komori, M. Kanazawa, K. Noda, N. Miyahara, H. Itoh, M. Endo, and T. Kanai. Irradiation system for himac. *J Radiat Res.* 48(Suppl.):A15-25, 2007.
- [6] A. D. Jensen, M. W. Münter, and J. Debus. Review of clinical experience with ion beam radiotherapy. *Br J Radiol. Advance online publication*. doi:10.1259/bjr/71511359, 2011.
- [7] D. Schulz-Ertner, A. Nikoghosyan, B. Didingr, M. Münter, O. Jäkel, C. P. Karger, and J. Debus. Therapy strategies for locally advanced adenoid cystic carcinomas using modern radiation therapy techniques. *Cancer*. 104(2):338-344, 2005.
- [8] D. Schulz-Ertner, A. Nikoghosyan, H. Hof, B. Didingr, S. E. Combs, O. Jäkel, C. P. Karger, L. Edler, and J. Debus. Carbon ion radiotherapy of skull base chondrosarcomas. *Int J Radiat Oncol Biol Phys.* 67(1):171-177, 2007.
- [9] D. Schulz-Ertner, C. P. Karger, A. Feuerhake, A. Nikoghosyan, S. E. Combs, O. Jäkel, L. Edler, M. Scholz, and J. Debus. Effectiveness of carbon ion radiotherapy in the treatment of skull-base chordomas. *Int J Radiat Oncol Biol Phys.* 68(2):449-457, 2007.
- [10] H. Tsujii, J. E. Mizoe, T. Kamada, M. Baba, S. Kato, H. Kato, H. Tsuji, S. Yamada, S. Yasuda, T. Ohno, T. Yanagi, A. Hasegawa, T. Sugawara, H. Ezawa, S. Kandatsu, K. Yoshikawa, R. Kishimoto, and T. Miyamoto. Overview of clinical experiences on carbon ion radiotherapy at nirs. *Radiother Oncol.* 73(Suppl. 2):S41-S49, 2004.
- [11] H. Tsujii, J. Mizoe, T. Kamada, M. Baba, H. Tsuji, H. Kato, S. Kato, S. Yamada, S. Yasuda, T. Ohno, T. Yanagi, R. Imai, K. Kagei, H. Kato, R. Hara, A. Hasegawa, M. Nakajima, N. Sugane, N. Tamaki, R. Takagi, S. Kandatsu, K. Yoshikawa, R. Kishimoto, and

- T. Miyamoto. Clinical results of carbon ion radiotherapy at nirs. *J Radiat Res (Tokyo)*. 48(Suppl. A):A1-A13, 2007.
- [12] S. E. Combs, M. Ellerbrock, T. Haberer, D. Habermehl, A. Hoess, O. Jäkel, A. Jensen, S. Klemm, M. Münter, J. Naumann, A. Nikoghosyan, S. Oertel, K. Parodi, S. Rieken, and J. Debus. Heidelberg ion therapy center (hit): Initial clinical experience in the first 80 patients. *Acta Oncol.* 49(7):1132-1140, 2010.
- [13] T. Haberer, J. Debus, H. Eickhoff, O. Jäkel, D. Schulz-Ertner, and U. Weber. The Heidelberg Ion Therapy Center. *Radiother Oncol.* 73(Suppl. 2):S186-S190, 2004.
- [14] S. E. Combs, O. Jäkel, T. Haberer, and J. Debus. Particle therapy at the heidelberg ion therapy center (hit) - integrated research-driven university-hospital-based radiation oncology service in heidelberg, germany. *Radiother Oncol.* 95(1):41-44, 2010.
- [15] O. Jäkel, G. H. Hartmann, C. P. Karger, P. Heeg, and J. Rassow. Quality assurance for a treatment planning system in scanned ion beam therapy. *Med Phys.* 27(7):1588-1600, 2000.
- [16] C. P. Karger, G. H. Hartmann, O. Jäkel, and P. Heeg. Quality management of medical physics issues at the german heavy ion therapy project. *Med Phys.* 27(4):725-736, 2000.
- [17] B. Arjomandy, N. Sahoo, X. R. Zhu, J. R. Zullo, R. Y. Wu, M. Zhu, X. Ding, C. Martin, G. Ciangaru, and M. T. Gillin. An overview of the comprehensive proton therapy machine quality assurance procedures implemented at the university of texas m. d. anderson cancer center proton therapy center-houston. *Med Phys.* 36(6):2269-2282, 2009.
- [18] C. P. Karger, O. Jäkel, H. Palmans, and T. Kanai. Dosimetry for ion beam radiotherapy. *Phys Med Biol.* 55:R193-R234, 2010.
- [19] M. Pijls-Johannesma, P. Pommier, and Y. Lievens. Cost-effectiveness of particle therapy: current evidence and future needs. *Radiother Oncol.* 89(2):127-134, 2008.
- [20] M. Durante and J. S. Loeffler. Charged particles in radiation oncology. *Nat Rev Clin Oncol.* 7:37-43, 2010.
- [21] O. Jäkel, B. Land, S. E. Combs, D. Schulz-Ertner, and J. Debus. On the cost-effectiveness of carbon ion radiation therapy for skull base chordoma. *Radiother Oncol.* 83:133-138, 2007.
- [22] T. Haberer, W. Becher, D. Schardt, and G. Kraft. Magnetic scanning system for heavy ion therapy. *Nuclear Instruments and Methods in Physics Research Section A.* 330(1-2):296-305, 1993.

- [23] S. Brons. Personal communication, 2012.
- [24] C. P. Karger, O. Jäkel, and G. H. Hartmann. A system for three-dimensional dosimetric verification of treatment plans in intensity-modulated radiotherapy with heavy ions. *Med Phys.* 26(10):2125-2132, 1999.
- [25] B. Hartmann, J. Telsemeyer, L. Huber, B. Ackermann, O. Jäkel, and M. Martišíková. Investigations of a flat-panel detector for quality assurance measurements in ion beam therapy. *Phys Med Biol.* 57:51-68, 2012.
- [26] B. J. McParland. *Nuclear Medicine Radiation Dosimetry: Advanced Theoretical Principles*. Springer, 2010.
- [27] A. Weiss. Neues leuchtschirmsystem für hochenergetische ionenstrahlen. Master's thesis, Fachbereich Physikalische Technik der Fachhochschule Wiesbaden, 2001.
- [28] *Phosphor Screens*. Proxitronic, Robert-Bosch-Str. 34, D-64625 Bensheim, Germany.
- [29] Iidc 1394-based digital camera specification version 1.30. Technical report, 1394 Trade Association, 2000.
- [30] *IEEE1394 Digital CCD Camera C4742-80-12AG Instruction Manual*. Hamamatsu Photonics Deutschland GmbH, Arzbergerstr. 10, D-82211 Herrsching am Ammersee, Germany.
- [31] *Automatic Iris ER Series Lenses Instruction Manual*. Pentax Ricoh Imaging GmbH, Julius-Vosseler-Strasse 104, 22527 Hamburg, Germany.
- [32] C. R. Baker and I. Ulrich. Cmu 1394 digital camera driver version 6.4.6. Driver and C++ software library for cameras that comply with the 1394 Digital Camera Specification. Carnegie Mellon University, The Robotics Institute. [<http://www.cs.cmu.edu/iwan/1394/index.html>], 2011.
- [33] Qt libraries version 4.7.3 for windows (vs 2008). Cross-platform application and UI framework. Nokia corporate. [<http://qt.nokia.com/>], 2011.
- [34] U. Rathmann and J. Wilgen. Qwt - qt widgets for technical applications version 5.2.2. Graphics extension to the Qt GUI application framework . [<http://qwt.sourceforge.net/>], 2011.
- [35] S. Leffler. Libtiff - tiff library and utilities version 1.42. Software providing support for the Tag Image File Format (TIFF). Silicon Graphics, Inc. [<http://www.libtiff.org/>], 2005.
- [36] Microsoft visual studio c++ 2008 express edition. Development environment for c++. Microsoft Corporation. [<http://msdn.microsoft.com/en-us/express/future/default>], 2008.

- [37] S. P. Platt, B. Cassels, and Z. Torok. Development and application of a neutron sensor for single-event effects analysis. *Journal of Physics: Conference Series*. 15:172-176, 2005.
- [38] H. Haferkorn. *Optik (3rd ed.)*. Barth, 1994.
- [39] J. Nolting and C. Lempart. Bündelbegrenzung - teil 1: Die grundbegriffe. *DOZ*. 9-2007:50-55, 2007.
- [40] D. Kühlke. *Optik - Grundlagen und Anwendungen (2nd ed.)*. Harri Deutsch, 2007.
- [41] *FOLNET 1 / 2 / 3*. Lightec GmbH, Rüdelsweg 3, D - 96050 Bamberg, Germany.
- [42] O. Jaekel, C. Jacob, D. Schardt, C. P. Karger, and G. H. Hartmann. Relation between carbon ion ranges and x-ray ct numbers. *Med Phys*. 28(4):701-703, 2001.
- [43] W. H. Press, S. A. Teukolsky, W. T. Vetterling, and B. P. Flannery. *Numerical Recipes - The art of scientific computing (3rd ed.)*. Cambridge University Press, 2007.
- [44] L. Ma, P. B. Geis, and A. L. Boyer. Quality assurance for dynamic multileaf collimator modulated fields using a fast beam imaging system. *Med Phys*. 24(8):1213-1220, 1997.
- [45] J. S. Li, A. L. Boyer, and C. M. Ma. Verification of imrt dose distributions using a water beam imaging system. *Med Phys*. 28 (12):2466-2474, 2001.
- [46] M. P. Petric, J. L. Robar, and B. G. Clark. Development and characterization of a tissue equivalent plastic scintillator based dosimetry system. *Med Phys*. 33(1):96-105, 2005.
- [47] M. Partridge, P. M. Evans, and M. A. Mosleh-Shirazi. Linear accelerator output variations and their consequences for megavoltage imaging. *Med Phys*. 25(8):1443-1452, 1998.
- [48] V. Collomb-Patton, P. Boher, T. Leroux, J. M. Fontbonne, A. Batalla, and A. Vela. Dosimap: A high-resolution 2-d tissue equivalent dosimeter for linac qa and imrt verification. *Radiat Prot Dosimetry*. 131(1):100-109, 2008.
- [49] T. Wiezorek, N. Banz, M. Schwedas, M. Scheithauer, H. Salz, D. Georg, and T. G. Wendt. Dosimetric quality assurance for intensity-modulated radiotherapy. *Strahlenther Onkol*. 181:468-474, 2005.
- [50] A. F. Monti and G. Frigerio. Dosimetric verification of 6 and 18 mv intensity modulated photon beams using a dedicated fluoroscopic electronic portal imaging device (epid). *Radiation Oncol*. 81:88-96, 2006.
- [51] S. N. Boon, P. van Luijk, J. M. Schippers, H. Meertens, J. M. Denis, S. Vynckier, J. Medin, and E. Grusell. Fast 2d phantom dosimetry for scanning proton beams. *Med Phys*. 25 (4):464-475, 1998.

- 
- [52] J. M. Schippers, S. N. Boon, O. C. Dermois, and H. H. Kiewiet. Beam instrumentation in a multidisciplinary accelerator facility. *Nuclear Instruments and Methods in Physics Research B* 139:389-393, 1998.
- [53] J. Barkhof, G. Schut, J. B. Flanz, M. Goitein, and J. M. Schippers. Verification of the alignment of a therapeutic radiation beam relative to its patient positioner. *Med Phys.* 26(11):2429-2437, 1999.
- [54] J. M. Schippers, S. N. Boon, and P. van Luijk. Applications in radiation therapy of a scintillating screen viewed by a ccd camera. *Nuclear Instruments and Methods in Physics Research A* 477:480-485, 2002.
- [55] S. N. Boon, P. van Luijk, T. Böhringer, A. Coray, A. Lomax, E. Pedroni, B. Schaffner, and J. M. Schippers. Performance of a fluorescent screen and ccd camera as a twodimensional dosimetry system for dynamic treatment techniques. *Med Phys.* 27 (10):2198-2208, 2000.
- [56] T. Furukawa, N. Saotome, T. Inaniwa, S. Sato, K. Noda, and T. Kanai. Delivery verification using 3d dose reconstruction based on fluorescence measurement in a carbon beam scanning irradiation system. *Med Phys.* 35(6):2235-2242, 2008.
- [57] A. Mairani, S. Brons, F. Cerutti, A. Fassò, A. Ferrari, M. Krämer, K. Parodi, M. Scholz, and F. Sommerer. The fluka monte carlo code coupled with the local effect model for biological calculations in carbon ion therapy. *Phys Med Biol.* 55(15):4273-4289, 2010.
- [58] S. Beddar, L. Archambault, N. Sahoo, F. Poenisch, G. T. Chen, M. T. Gillin, and R. Mohan. Exploration of the potential of liquid scintillators for real-time 3d dosimetry of intensity modulated proton beams. *Med Phys.* 36(5):1736-1743, 2009.
- [59] S. Safai, S. Lin, and E. Pedroni. Development of an inorganic scintillating mixture for proton beam verification dosimetry. *Phys Med Biol.* 49:4637-4655, 2004.

## A. Addendum

### **Installation of the 3rd Party Components in the Image Acquisition Software and Integration into Visual Studio C++ Express[VS]**

#### 1. Steps to run the .exe File

To use the image acquisition software the steps described in this section are sufficient. If the aim is to adapt the software, the instructions in 1.2 will have to be used instead.

Download: Download Microsoft Visual Studio C++ 2008 Express Edition from:

<http://1/msdn.microsoft.com/en-us/express/future/bb421473>.

Installation: Install with no additional features. Register. This also automatically installs Microsoft Platform SDK v6.0A.

Configuration:

Copy the folder Rules provided with the image acquisition software into the folder Microsoft Visual Studio 9.0.

Copy the .dll files provided with the image acquisition software into:

C:\WINDOWS\system32.

#### 2. Steps to build the Project

The steps described in this section were used for development of the image acquisition software (it is used with LibTIFF 1.42). The paths refer to those automatically set in installation.

##### a) CMU 1394 Digital Camera Driver

Download Download the latest version from (here: 6.4.6, select the .exe file):

<http://www.cs.cmu.edu/~iwan/1394/download.html>.

Installation:

Make sure your camera is plugged in, follow the setup procedure and select Update driver for attached devices. 1394camera.dll and 1394camerad.dll are placed in C:\WINDOWS\system32 automatically during installation.

If the camera cannot be plugged in during installation, it can be reinstalled after it is plugged in. However, if the camera driver has to be updated manually, instructions can be found on the provider website:

<http://www.cs.cmu.edu/~iwan/1394/install.html>.



---

Environment Variables: Start => control panel => system => advanced => environment variables => system variables, add: 1394DIR C:\Programme\CMU\1394Camera

b) Visual Studio C++ Express Part A

Download: Download Microsoft Visual Studio C++ 2008 Express Edition from:  
<http://msdn.microsoft.com/en-us/express/future/bb421473>.

Installation:

Install with no additional features. Register.

This also automatically installs Microsoft Platform SDK v6.0A. In Visual Studio it can easily be checked which SDK is currently used: Open a project => in the menu bar choose project => properties => configuration properties => debugging => environment => macros => check the macros WindowsSdkDir and FrameworkSDKDir => if the desired path is not shown, adapt the registration keys WindowsSdkDir and FrameworkSDKDir: Run regedit => HKEY\_LOCAL\_MACHINE (later repeat these steps for HKEY\_CURRENT\_USER if applicable) => Software => Microsoft => Microsoft SDKs => Windows => adapt: Current Install Folder, Current Version and Product Version if applicable

Environment Variables: Start => control panel => system => advanced => environment variables => system variables => edit PATH, add:  
C:\Programme\MicrosoftVisualStudio9.0\VC\bin

c) QT

Download:

If possible, get the folder 4.7.3-vc that was used together with the Image acquisition software before. Set the environment variables as described below and go on with the last step of the configuration.

Download qt-win-opensource-4.7.3-vs2008.exe from:  
<http://qt.nokia.com/qt/source>

Installation: Install with the preset settings.

Environment Variables:

Start => control panel => system => advanced => environment variables  
=> system variables, add: QTDIR C:\Qt\4.7.3-vc\qt INCLUDE \%  
QTDIR\%\include LIB \%QTDIR\%\lib  
=> edit PATH, add: PATH \%QTDIR\%\bin

Configuration:

For integration of QT into Visual Studio, instructions on the following web-sites have been used:

<http://fakguen.wordpress.com/2008/07/14/qt-440-visual-studio-integr>

[http://dcsoft.com/community\\_server/blogs/dcsoft/archive/2009/03/06/how-to-setup-qt-4-5-visual-studio-integration.aspx](http://dcsoft.com/community_server/blogs/dcsoft/archive/2009/03/06/how-to-setup-qt-4-5-visual-studio-integration.aspx)

<http://mm-werkstatt.informatik.uni-augsburg.de/documents/tutorials/qt2005.pdf>

Copy the whole installed subfolder of C:\Qt, paste a copy back into C:\Qt and rename the copy version-vc, the original folder will be used with QT Creator and the new folder will be rebuilt compatible to Visual Studio.

Now, open the Visual Studio console:

```
c:\> cd c:\qt\4.7.3-vc
```

```
c:\qt\4.5.x-vc> configure -no-qt3support -no-webkit -platform win32-  
msvc2008 -no-dbus (Can be adapted according to: http://qt.nokia.com/doc/qtextended4.4/buildsystem/over-configure-options-1.html)  
Configure generates nmake compatible makefiles to build the li-  
braries.
```

```
c:\qt\4.5.x-vc\qt> nmake This will take some time and builds the  
specified Qt DLL's and libraries with Visual Studio. If an error occurs,  
regenerate the makefiles.
```

Copy the following .dll files from C:\Qt\4.7.3-vc\bin into

C:\WINDOWS\system32: QtGuid4.dll QtCored4.dll QtGui4.dll QtCore4.dll

If you want to use Qt Creator instead of Visual Studio to compile, you need to exchange these for the .dll files from the original folder, respectively.

d) QWT

Download: Download version 5.2.2 from: <http://qwt.sourceforge.net/>

Environment Variables:

Start => control panel => system => advanced => environment variables =>  
system variables, add: QWTDIR : C:\qwt

=>edit PATH, add: PATH \%QWTDIR%\lib

Configuration:

---

For configuration of Qwt, instructions on the following website have been used: <http://fakguen.wordpress.com/2008/08/04/qwt-bibliothek/>

Check and edit qwtconfig.pri: #CONFIG += release\_debug and #CONFIG += build\_all Likewise this command has to be commented out by adding#: CONFIG += release

Now, open the Visual Studio console: c:\> cd C:\qwt qmake qwt.pro nmake

Copy the following .dlls from C:\qwt\lib to \%QTDIR%\bin: qwt5.dll and qwt5d.dll

Copy the following files into \%QTDIR%\lib: qwt5.exp, qwt5d.exp, qwt5d.ilc, qwt5.lib, qwt5d.lib and qwt5d.pdb

#### e) Visual Studio C++ Express Part B

Configuration:

Add folders to the project directories Tools => Options => Projects and Solutions => VC++ directories => add:

include files:

\\$(QTDIR)\include, \path{\\$(QTDIR)\include\Qt}, \\$(QTDIR)\include\QtCore

\\$(WindowsSdkDir)\include, \\$(WindowsSdkDir)\include\gl and \\$(FrameworkSDKDir)\include

\\$(1394dir)\include

library files:

\\$(QTDIR)\lib

\\$(WindowsSdkDir)\lib and \\$(FrameworkSDKDir)\lib

\\$(1394DIR)\lib

\\$(QWTDIR)\lib

executable files: \\$(WindowsSdkDir)\bin and \\$(FrameworkSDKDir)\bin

source files: \\$(QWTDIR)\src

Configure project properties of the scintillator project:

Switch to Configuration => Debug Librarian => Input => add into Additional Dependencies: qtmaind.lib QtGuid4.lib QtCored4.lib 1394Cam-erad.lib

Switch to Configuration => Release Librarian => Input => add into Additional Dependencies: qtdmain.lib QtGui4.lib QtCore4.lib 1394Camera.lib

Custom Build Rules:

Create a Custom Build Rule for handling .ui files:

Open a project => right click on project => Custom Build => new custom build rule

=> fill out this form:

Display Name: ui\_rule

File Name: ui\_rule

Directory: C:\Programme\MicrosoftVisualStudio9.0\Rules

=> Add Build Rule:

Display Name: Compile QT UserInterface File (\*.ui)

Execution Description: Build UI File ui\\_\$(InputName).h

Outputs: ui\\_\$(InputName).h

Command Line: \$(QTDIR)/bin/uic.exe "\$(InputPath)" -oui\_\$(InputName).h

File Extensions: \*.ui

Name: UI

To use this rule in all project files: Tools => Options => Projects and Solutions => VC++ Project Settings => add into Rule File Search Paths: C:\Programme\MicrosoftVisualStudio9.0\Rules

For each header file containing macros like Q\_OBJECT an additional Custom Build Step needs to be created: Right click on header => Properties => Configuration Properties => Custom Build Step => add:

Command Line: \\$(QTDIR)\bin\moc.exe "\\$(InputPath)" -o "\\$(InputDir) moc\\_\$(InputName).cpp"

Description: Performing moc on \$(InputName).h

Outputs: \\$(InputDir) moc\\_\$(InputName).cpp

## Acknowledgements

Last, but not least, I want to thank everyone, who contributed to this work, either academically or providing personal support. In particular, I would like to express my personal gratitude to:

My supervisor Prof. Dr. Christian Karger, who always finds time for fruitful discussions, helpful explanations and a very fast and constructive revision. Thanks for having me in your working group.

All medical and accelerator physicists at HIT, for support and helpful discussion before, during and after measurements and especially for the much appreciated help when measurements didn't work as planned. I particularly want to express my gratitude to Jakob Naumann, Andreas Peters, Stephan Brons, Ralf Panse, Marcus Winter, Jochen Schreiner and Thomas Haberer. Additionally, I want to thank all the medical physicists for sharing your knowledge during QA, it was always nice to work with you. I also want to thank Bernadette and the rest of FS2 for discussing our experiences with QA and taking each others shifts when needed.

Prof. Dr. W. Schlegel for providing great working conditions for his division of the DKFZ.

Prof. Dr. Uwe Oelfke for quickly helping out as first referee of my thesis.

My TAC members and thesis committee for kindly accepting these tasks.

My working group, current, former and adopted members included, because they are nice to hang out with in and out side the office, and for giving support whenever needed. Special thanks go to my sport buddies Carine and Christin and to Paola, Ina and Torsten for always having a sympathetic ear.

I also want to sent an aloha to the beam team and Asja and Siri for a unique experience.

Special thanks goes to my friends for bearing with me whenever I was stressed out and of course especially for their support during the final stages of this work. A big thank goes to Ina, Andreas and Holger for providing a ton of last minute support. A big hug also goes to Ines for being my exam buddy.

Most of all, I want to thank my parents and family for their termless support in every respect.

